Title: A CRISPR-screen in intestinal epithelial cells identifies novel factors for polarity and apical transport

Authors: Katharina MC Klee[1,2+], Michael W Hess[3+], Michael Lohmüller[4], Sebastian Herzog[4], Kristian Pfaller[3], Thomas Müller[2], Georg F Vogel[1,2*] and Lukas A Huber[1];

Affiliations: [1] Institute of Cell Biology, Medical University of Innsbruck, Austria

[2] Department of Paediatrics I, Medical University of Innsbruck

[3] Institute of Histology and Embryology, Medical University of Innsbruck, Austria

[4] Institute of Developmental Immunology, Medical University of Innsbruck, Austria

[+] Authors contributed equally to this work

Conflict of interest: The authors have declared that no conflict of interest exists.

Keywords: CRISPR; loss of function screen; epithelial polarity; transport; electron microscopy; microvillus inclusion disease;

*** Corresponding Author:**

Georg F Vogel (contact and submitting author)
Institute of Cell Biology
Medical University Innsbruck
Innrain 80-82
6020 Innsbruck
Austria
georg.vogel@i-med.ac.at
phone: +43 512 504 82184
fax: +43 512 504 25450

Abstract

Epithelial polarization and polarized cargo transport are highly coordinated and interdependent processes. In our search for novel regulators of epithelial polarization and protein secretion, we used a genome-wide CRISPR/Cas9 screen and combined it with an assay based on fluorescence-activated cell sorting (FACS) to measure the secretion of the apical brush border hydrolase dipeptidyl peptidase 4 (DPP4). In this way, we performed the first CRISPR screen to date in human polarized epithelial cells. Using high-resolution microscopy, we detected polarization defects and mislocalization of DPP4 to late endosomes/lysosomes after knock-down of TM9SF4, anoctamin 8, and ARHGAP33, confirming the identification of novel factors for epithelial polarization and apical cargo secretion. Thus, we provide a powerful tool suitable for studying polarization and cargo secretion in epithelial cells. In addition, we provide a dataset that serves as a resource for the study of novel mechanisms for epithelial polarization and polarized transport and facilitates the investigation of novel congenital diseases associated with these processes.

Introduction

Epithelia are highly specialized tissues that line inner and outer surfaces of various organs of metazoans, performing absorption, secretion, and barrier functions. During polarization epithelial cells assume their characteristic shape, by building specialized apical- and basolateral plasma membrane (PM) domains (Rodriguez-Boulan and Macara, 2014; Apodaca et al., 2012), which are separated by junctional complexes and characterized by a specific composition of lipids and proteins (Martin-Belmonte et al., 2007). The asymmetric distribution of polarity complexes and the mutual exclusion of proteins from one domain, by proteins from the other domain are critical for the maintenance of apico- basolateral domains at the cell cortex (Rodriguez-Boulan and Macara, 2014; Román-Fernández and Bryant, 2016). Additionally, tightly orchestrated transport mechanisms and machineries, as Rab-GTPases, motor proteins, soluble NSF attachment receptor (SNARE)-proteins and specific adapter proteins, ensure the establishment and maintenance of specialized membrane domains (Gaisano et al., 1996; Low et al., 1996; Weimbs et al., 1997; Li et al., 2002).

Defects in polarization and polarized traffic often cause diseases, such as congenital diarrhea and enteropathies (Thiagarajah et al., 2018; Canani et al., 2010; Apodaca et al., 2012). Microvillus inclusion disease is an autosomal-recessive enteropathy (Cutz et al., 1989), characterized by intractable diarrhea in neonates (Cutz et al., 1989; Ruemmele et al., 2006). Enterocytes of MVID-patients show loss of brush-border microvilli, formation of so-called microvillus-inclusions and subapical accumulation of so-called “secretory granules” (Cutz et al., 1989; Phillips et al., 2000). Our studies identified mutations in *MYO5B*, *STX3* and *STXBP2* to be causative for MVID (Müller et al., 2008; Ruemmele et al., 2010; Wiegerinck et al., 2014; Vogel et al., 2017b); they revealed that a molecular transport machinery involving myosin Vb (myo5b), the small Rab-GTPases Rab11a and Rab8a, the t-SNARE syntaxin3 (stx3) and the v-SNAREs slp4a and vamp7 is essential for apical cargo delivery (Vogel et al., 2015b, 2017b). This cascade is required for the delivery of apical transmembrane transporters that are important for proper physiological function of enterocytes, such as sodium-hydrogen exchanger 3 (NHE3), glucose transporter 5 (GLUT5) and cystic fibrosis transmembrane conductance receptor (CFTR), but not for dipeptidyl-peptidase-4 (DPP4), sucrase-isomaltase (SI) and amino-peptidase-N (APN). This suggests the presence of additional trafficking routes and transport mechanisms for these apical cargos.

Since molecular signals for apical cargo sorting and transport are believed to be highly diverse, various mechanisms have been proposed to underly epithelial protein secretion (Levic and Bagnat, 2021). A common, characteristic feature of apical cargo is the presence of post-translational modifications, such as N- and O-linked glycosylations that are recognized by specific lectins, as well as GPI-anchors that allow sorting into cholesterol-rich lipid

microdomains (Weisz and Rodriguez-Boulan, 2009; Zurzolo and Simons, 2016). Additionally, recent studies have proposed that protein oligomerization coincides with sorting into specialized membrane domains in the *trans*-Golgi network (TGN), which depends on the pH-regulation of the TGN lumen (Levic and Bagnat, 2021; Levic et al., 2020).

To uncover protein functions for a wide range of cellular processes, genome-wide clustered regularly interspaced short palindromic repeats (CRISPR) mediated screens have advanced to a state-of-the-art strategy (Shalem et al., 2014, 2015; Kampmann, 2018). In addition to their application to understanding the regulation of tumor biology, viral infection, or miRNA processing, CRISPR-mediated screening approaches have recently proven highly effective in discovering novel factors for intracellular protein trafficking and secretion (He et al., 2021; Zhu et al., 2021; Hutter et al., 2020; Stewart et al., 2017; Popa et al., 2020; Bassaganyas et al., 2019). Additionally, the CRISPR-Cas9 technology has been successfully used in madine-darby canine kidney (MDCK) cells with the generation of a collection of Rab-GTPase knockouts, which has provided great value for phenotypic analyses of Rab-KOs in epithelial cells (Homma et al., 2019).

In this study, we employed the CRISPR-screening technology as an unbiased experimental strategy to uncover novel regulators of epithelial cell polarization and trafficking by investigating factors required for the apical delivery of DPP4. The brush-border hydrolase DPP4 is a type II transmembrane protein. It is heavily modified with N- and O-linked glycans in its extracellular domain (Misumi et al., 1992; Baricault et al., 1995; Fan et al., 1997), which have been suggested to be critical apical sorting determinants of DPP4 (Alfalah et al., 2002). Even though several studies have suggested diverse trafficking routes for DPP4, the mechanisms and protein-machineries underlying these processes remain enigmatic so far (Casanova et al., 1991; Baricault et al., 1993; Low et al., 1992; Sobajima et al., 2015).

Here, we conducted the first CRISPR-screen in polarized human epithelial cells to date. We present an experimental strategy for applying the CRISPR screening system in polarized epithelial cells to study novel protein functions. We have developed an easy to use and adaptable, FACS-based assay to measure the efficiency of protein secretion in polarized epithelial cells after genome editing. In combination with a detailed characterization of selected proteins by immunofluorescence and cryo-based electron microscopy, we have identified novel factors required for proper apico-basolateral polarization and secretion of apical cargo. Therefore, our dataset serves as a foundation for future studies aimed at deciphering novel mechanisms underlying epithelial polarization and polarized cargo transport. In addition, it provides a powerful resource for the investigation and validation of new congenital disease genes to be identified.

Results

Development of a genome-wide CRISPR-screen to identify factors required for plasma membrane localization of the apical cargo DPP4

We established an unbiased CRISPR-Cas9-loss of function screen to define factors involved in surface targeting of the apical model cargo DPP4 in the enterocyte like colon carcinoma cell line, CaCo2 (Fig. 1). DPP4 is a type 2 transmembrane protein, that can be detected with antibodies binding to the extracellular C-terminus of the protein (Fig. 1 A). We made use of this feature to read out the efficiency of endogenous DPP4 surface delivery by fluorescence activated cell sorting (FACS) in CaCo2 cells after epithelial polarization. Here, we used a period of 18 to 21 days, during which surface DPP4 signal is significantly increased in the course of cell surface expansion and specialized polarized trafficking processes (Fig. 1 B). In this context, we aimed to define factors required for apical membrane differentiation and cargo trafficking, thereby leading to a strong reduction of DPP4 after surface polarization. First, we generated Cas9-expressing CaCo2 cells and then transduced two biological replicates at a low multiplicity of infection (MOI) (0.2) using the human lentiviral GeCKOv2 CRISPR-library, selecting for successful viral integration with antibiotic treatment with Puromycin. We then seeded the infected CaCo2 cultures at high density and allowed the confluent monolayers to further polarize and differentiate for 18 days. Next, polarized cells were detached, stained for endogenous DPP4, and subjected to FACS, separating those cells with only 10% of surface signal left, due to CRISPR-targeting (Fig. 1 C and D). To determine the abundance of gRNAs in sorted versus unsorted cell populations, genomic DNA was isolated and read counts were determined by next generation sequencing. Subsequent analysis using GenePattern and Galaxy analysis tools enabled the identification of 89 gRNAs significantly enriched in the sorted cell population ($p<0.05$) and represented genes whose downregulation had resulted in reduced DPP4 surface release (Fig. 1 D and E; Table S1 A and B).

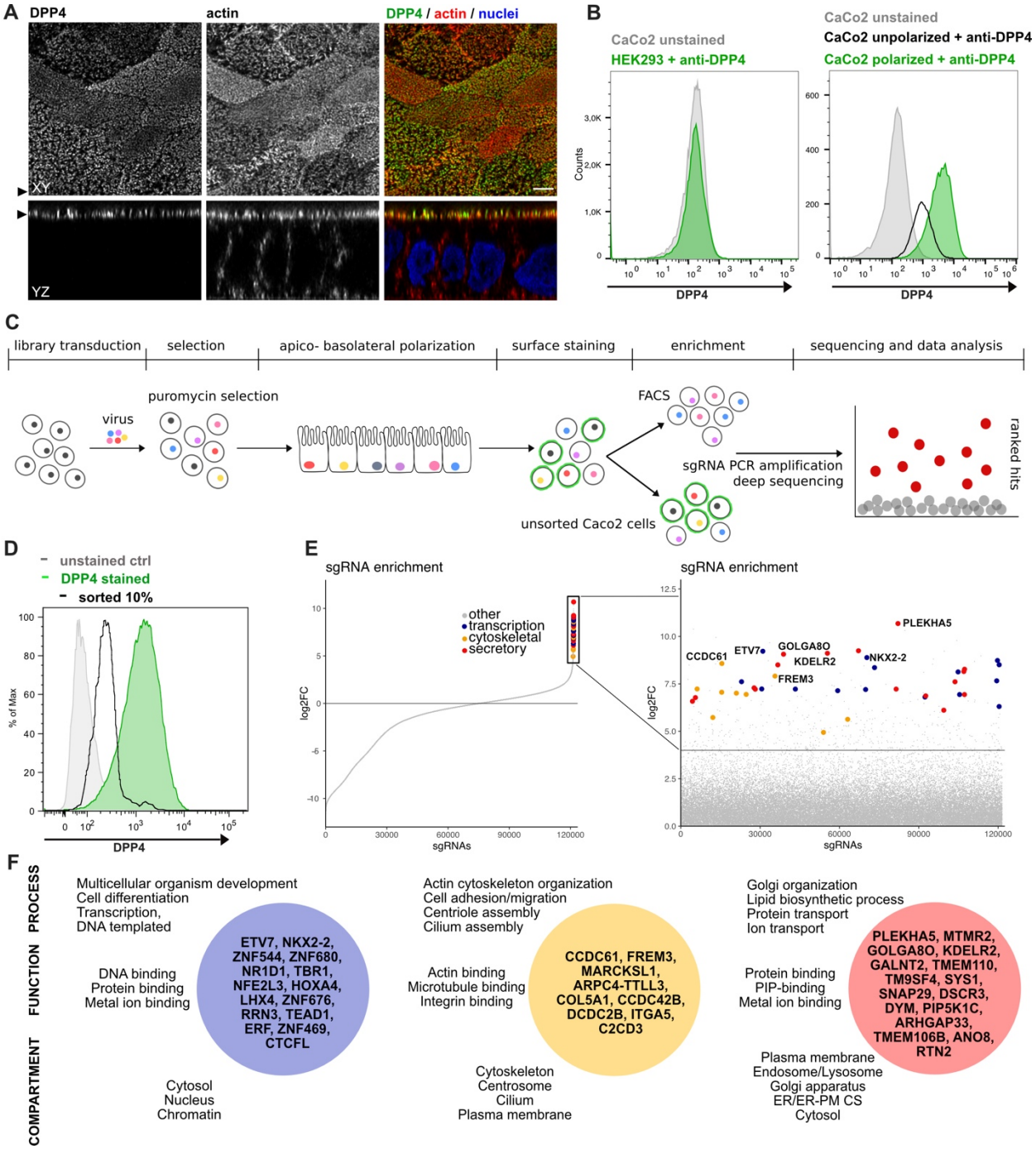

Figure 1. A CRISPR mediated loss of function screen in polarized enterocytes. A. Dipeptidylpeptidase 4 (DPP4) localizes to the apical brush-border of polarized enterocytes and can be detected with a specific antibody, at its extracellular stalk domain. Top-view (XZ) and lateral view (YZ) of a polarized CaCo2 monolayer. Scale = 5 µm **B.** During polarization, apical DPP4 is increased due to polarized traffic and surface expansion, which can be measured by flow cytometry (right panel, CaCo2 unpolarized versus polarized). HEK293T cells, not expressing DPP4, serve as quality control for staining specificity. **C.** CaCo2-Cas9 cells are transduced with the lentiGuide-Puro library and selected with Puromycin. After selection CaCo2 cells are seeded to confluent monolayers and cultured for apico-basolateral polarization. Subsequently cells are detached, stained, and subjected to fluorescence

activated cell sorting (FACS). Sorted and unsorted control cells are processed for gDNA extraction and genomically integrated CRISPR-constructs are amplified by PCR. Finally, PCR products of sorted and unsorted cell populations are analyzed by next generation sequencing and sgRNAs are ranked by their enrichment in the sorted vs. unsorted cell polpulation. **D.** Sorting was performed for 10% of the cells, with lowest surface-signal intensity, thereby enriching for the cell population that had lost 90% of surface DPP4 signal, due to efficient CRISPR targeting. **E.** 89 single guide RNAs were significantly enriched in the sorted cell population. **F.** Factors enriched in the sorted cell population could functionally be associated with secretory traffic, cytoskeletal architecture or transcription, in a manual gene-ontology analysis.

A genome-wide CRISPR-screen in polarized enterocytes identifies factors associated with secretory traffic

Next, we wanted to get a comprehensive overview on the gene classes represented in our list of enriched gRNAs. However, automated KEGG pathway and gene enrichment analyses of our results were insufficient. Hence, we manually analyzed the 89 identified genes for common gene ontology (GO)-terms and grouped them accordingly. We listed three GO-terms from each category (biological process, molecular function, cellular compartment) for each hit, including the most common GO-terms captured by the QuickGO-search database, focusing on including GO-terms that indicate a role in the secretory pathway (Table S1 C).

Our analysis highlighted several genes, with functions related to the organization of the secretory pathway (Fig. 1 E and F; Fig. 2 A), including general organization and maintenance of organelles such as the endoplasmic reticulum (ER), the Golgi apparatus or protein transport at early steps of the secretory pathway (e.g., *KDELR2, RTN2, GOLGA8O*). Further, identified hits were related to protein modification and transport at *cis*- and *trans*-Golgi compartments (*GALNT2, SYS1*), lipid-biosynthesis (*MTMR2, PIP5K1C*), vesicle fusion and endocytic recycling (*SNAP29, DSCR3*). Interestingly, we identified two genes associated with ER-plasma membrane (ER-PM) contact sites (*TMEM110, ANO8*). Furthermore, we found several factors required for various aspects of cytoskeletal organization such actin-filament organization/polymerization (e.g., *MARCKSL1, ARPC4-TTLL3*), cell adhesion (e.g., *ITGA5, FREM3, MPZ*) but also microtubule organizing centre (MTOC)/centriole- and cilium assembly and association (e.g., *CCDC61, CCDC42B, C2CD3*). Finally, we found numerous factors with functions related to DNA-templated transcription and cell-differentiation (e.g., *ETV7, NKX2-2, ERF*), as well as mRNA-processing/RNA-splicing (e.g., *SNRPE, SFSWAP*), translation (e.g., *RPL30, RPL2*) and DNA-repair/DNA-replication (e.g., *SFR1, ATAD5, REV1*) (Fig. 1 E and F; Fig. 2 A).

Overall, in a CRISPR-mediated loss-of-function screen, we identified a variety of factors that affect surface transmission of an apical model cargo protein, DPP4, at different cellular levels. This underscores the value of our dataset and approach to identify novel factors for secretory membrane trafficking in polarized epithelial cells.

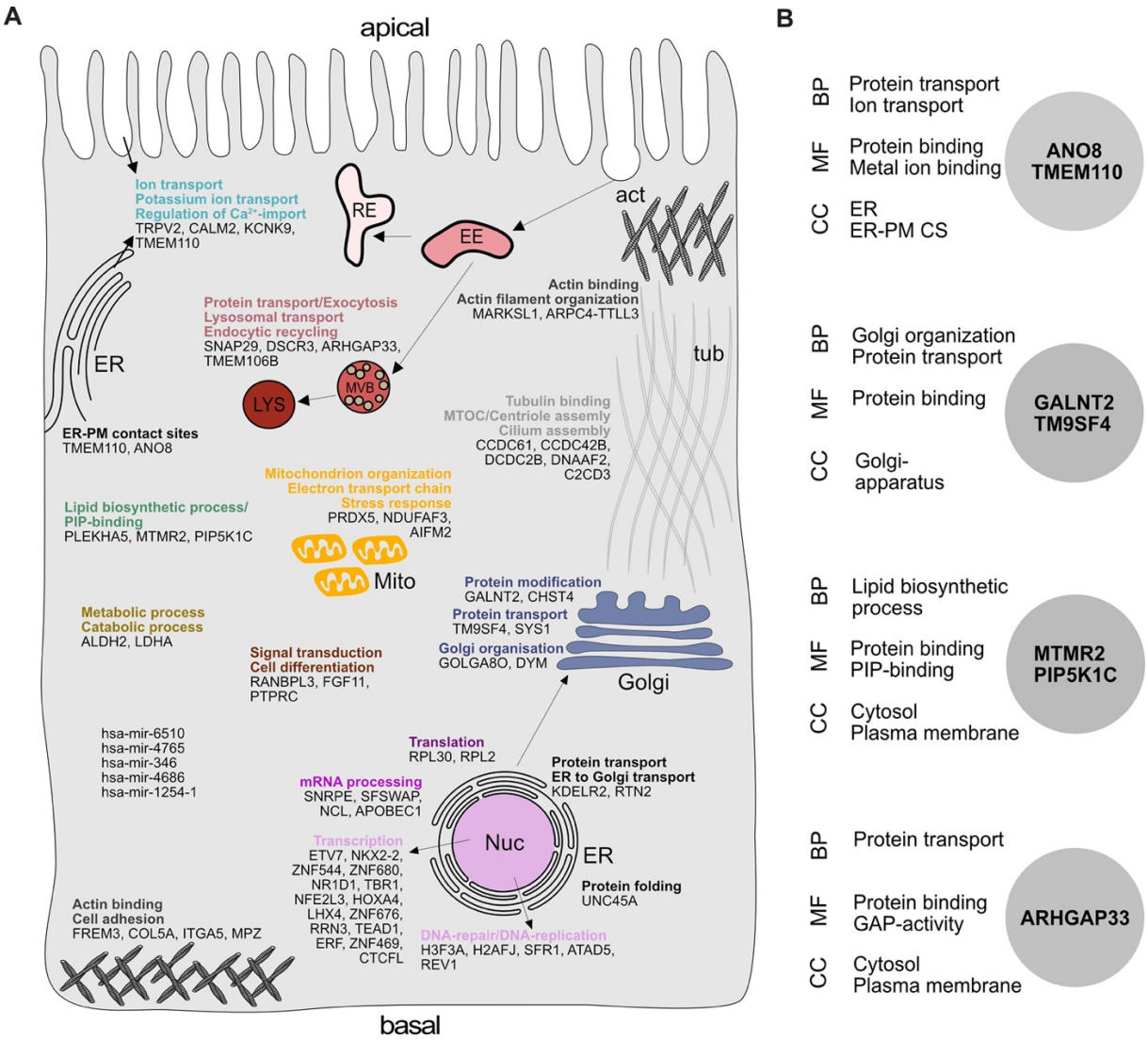

Figure 2. Gene-ontology analysis of hits obtained in a CRISPR-mediated loss of function screen in polarized CaCo2 cells. A. Schematic representation of significantly enriched genes obtained from a CRISPR-screening approach, grouped and organized according to their associated gene ontology (GO) terms. **B.** GO-association analysis of the 7 factors, that were chosen for CRISPR-screen readout-validation and further characterization. CC = cellular compartment, MF = molecular function, BP = biological process.

Novel factors for surface localization of the apical cargo DPP4

After setting up a CRISPR-mediated screening platform in polarized CaCo2 cells, we validated our screening approach by further characterizing potentially novel factors for apical cargo traffic and membrane polarization. Since we had identified several genes with functions related to secretory trafficking (Fig. 2 A), we chose 7 promising candidates for further analyses (Fig. 2 B). These factors function on various levels of the endomembrane system: the anoctamin family member anoctamin 8 (ANO8) and the stromal interaction molecule (STIM) enhancing tethering protein STIMATE (TMEM110) are required for establishment and maintenance of ER-PM contact sites, which in turn, have recently been shown to be required for apical PM-establishment in bile-canaliculi (Jha et al., 2019; Quintana et al., 2015; Chung et al., 2020).

The nonaspanin-family member TM9SF4 has been suggested to be required for transmembrane domain sorting in early steps of the secretory pathway but also in the generation of specialized membrane domains in the early *cis*- Golgi compartment (Perrin et al., 2015; Vernay et al., 2018; Yamaji et al., 2019). Polypeptide N-acetylgalactosaminyltransferase 2 (GALNT2) regulates O-linked glycosylation of transmembrane proteins in the Golgi, and was chosen as a candidate for screen validation, with a potentially global effect on secretory traffic (Wandall et al., 1997; Moremen et al., 2012). Sorting nexin 26 (SNX26/ARHGAP33) was included since it has been described as a GTPase activating protein for Cdc42, a major player in apical domain differentiation (Kim et al., 2013). Finally, we chose the lipid kinase subunit phosphatidylinositol 4-phosphate 5-kinase type-1 gamma (PIP5K1C) and the lipid phosphatase myotubularin-related protein 2 (MTMR2) for screen validation and further analysis- since they are known regulators of apical phosphatidylinositolphosphate (PIP)-pools (Xu et al., 2019; Román-Fernández et al., 2018).

We generated clonal knock-down (KD) cell lines of those candidates, using the CRISPR-technology and those gRNAs that had proven to efficiently target in our CRISPR-screen (Fig. 3 A). We then analyzed KD cell lines for surface localization of DPP4 by flow cytometry, using the previously described polarization assay from our CRISPR-screen (Fig. 3 B). These measurements showed that targeting of the selected candidates indeed leads to reduced surface localization of DPP4, but to varying degrees (Fig. 3 C). The strongest effect on DPP4 surface localization was caused by interference with PIP5K1C (~75% reduction), followed by TM9SF4, TMEM110 and GALNT2 (~50% reduction). Interestingly, ANO8-, MTMR2- and ARHGAP33-KDs showed the mildest phenotype (~30% reduction), (Fig. 3 B and C).

By growing KD cell lines of selected candidate genes and reanalyzing them for the effects of CRISPR targeting on PM localization of DPP4, we validated our primary CRISPR loss-of-function screen and thereby identified new players for surface localization of the apical cargo protein DPP4.

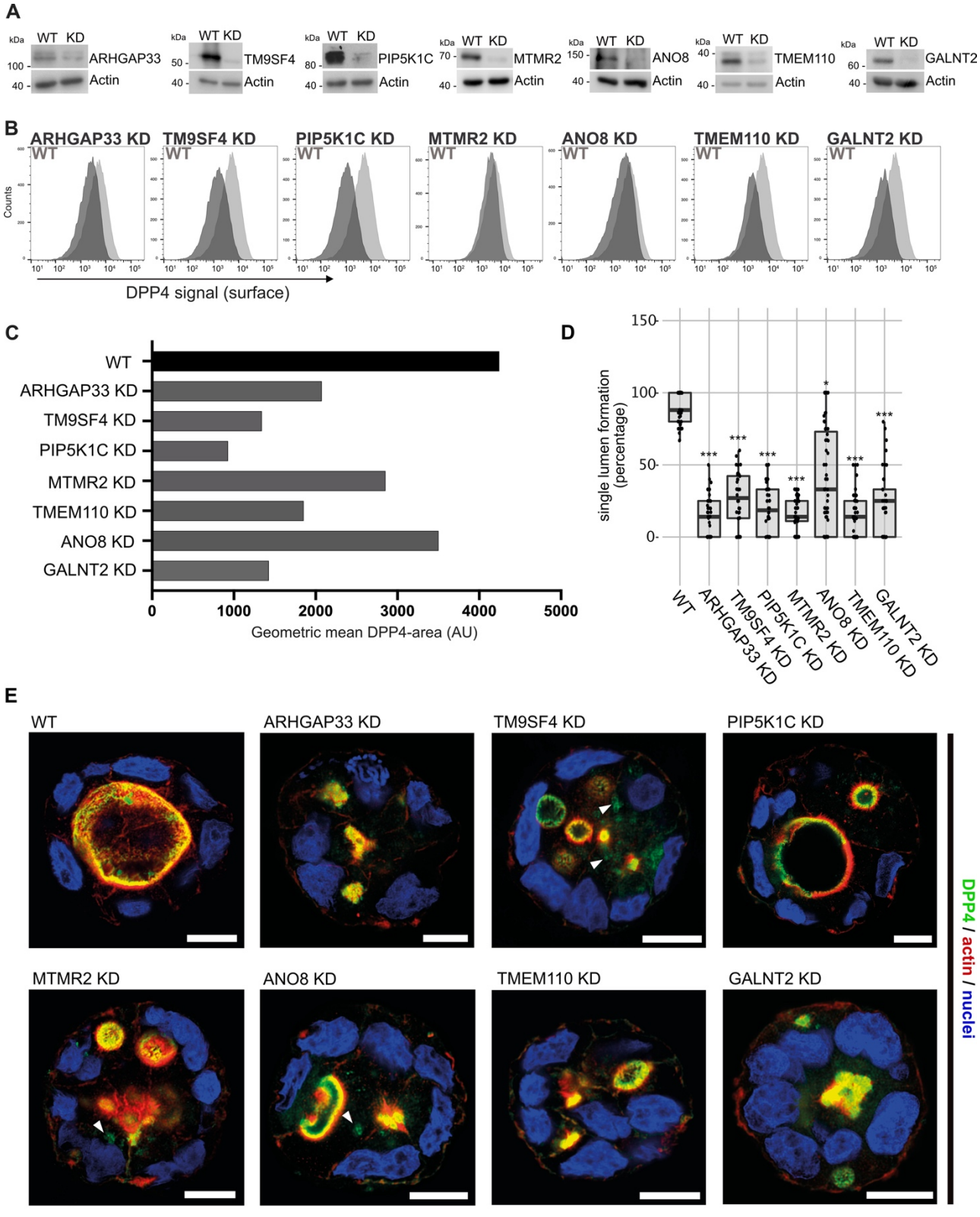

Figure 3. Validation of selected candidates, identified in a CRISPR-mediated loss of function screen. A. Generation of clonal knock-down (KD) cell lines of 7 candidates, chosen for primary CRISPR-screen validation and further analysis. Residual protein levels, if left, after CRISPR-targeting in the KD-clones were determined by Western-blotting by comparison to wildtype (WT) cells. Beta-actin was used as loading control. Molecular size markers are depicted in kDa. **B.** The effect of the respective KDs on DPP4 surface transport, in clonal KD

cell lines. Cell lines were polarized for 18 days and then subjected to flow cytometry, to determine the KD-effect on DPP4 surface targeting. **C.** Geometric means of DPP4-area (DPP4 intensity on the cellular surface) were determined of respective cell lines. All KD cell lines show varying extents of DPP4-surface reduction, with PIP5K1C-KD displaying the strongest and ANO8-KD the mildest effect. **D.** 3D cyst assay were performed with WT and KD cultures. Single central lumen formation was quantified. The percentage of cysts with a single central lumen is substantially decreased in the respective KD-clonal cells lines (dot box plot, Mann–Whitney U test ***$p < 0.001$). **E.** Immunofluorescence micrographs of 3D-cysts generated from WT and KD cell lines. All knockdown cell lines display the formation of multiple lumina or no lumina. DPP4 localizes to actin-rich structures in al KD cell lines and additionally, to intracellular, actin-negative compartments in TM9SF4-, MTMR2- and ANO8-KD clones (white arrowheads). Scale = 10 µm.

3D cyst models and high-resolution microscopy reveal novel factors for proper epithelial polarization

Because apical transport and the correct establishment of epithelial polarity are closely linked, we investigated the relevance of the newly identified factors for polarization. Therefore, we performed 3D cyst assays using WT and the corresponding KD cell lines (Fig. 3 D and E). Cysts were analyzed by immunofluorescence microscopy (IF) to determine the targeting of DPP4 to apical membrane domains (Fig. 3 E). We found that all KD cell lines had severe defects in the formation of a single, central lumen, but rather established multiple or no lumina (Fig. 3 D and E). Although DPP4 was localized in the apical PM domains in all KD-cell lines, TM9SF4-, MTMR2-, and ANO8-KD-cell lines additionally displayed aberrant intracellular accumulation of DPP4 (Fig. 3 E).

To characterize the involvement of the selected candidates in apico-basolateral polarization and apical transport in greater detail, we complemented fluorescence microscopy with cryo-based electron microcopy and investigated the ultrastructural phenotype and the subcellular distribution of selected marker molecules in the respective cell lines. For this, TM9SF4-, ANO8-, ARHGAP33-, TMEM110-, MTMR2-, PIP5K1C- and GALNT2-KD cell lines were grown for 18-21 days on permeable filter membranes to obtain fully polarized, differentiated 2D cell monolayers. Samples were then subjected to rapid cryo-fixation (high-pressure freezing and freeze-substitution) for transmission electron microscopy (TEM) or to conventional aldehyde fixation for scanning EM (SEM) and immunogold-TEM.

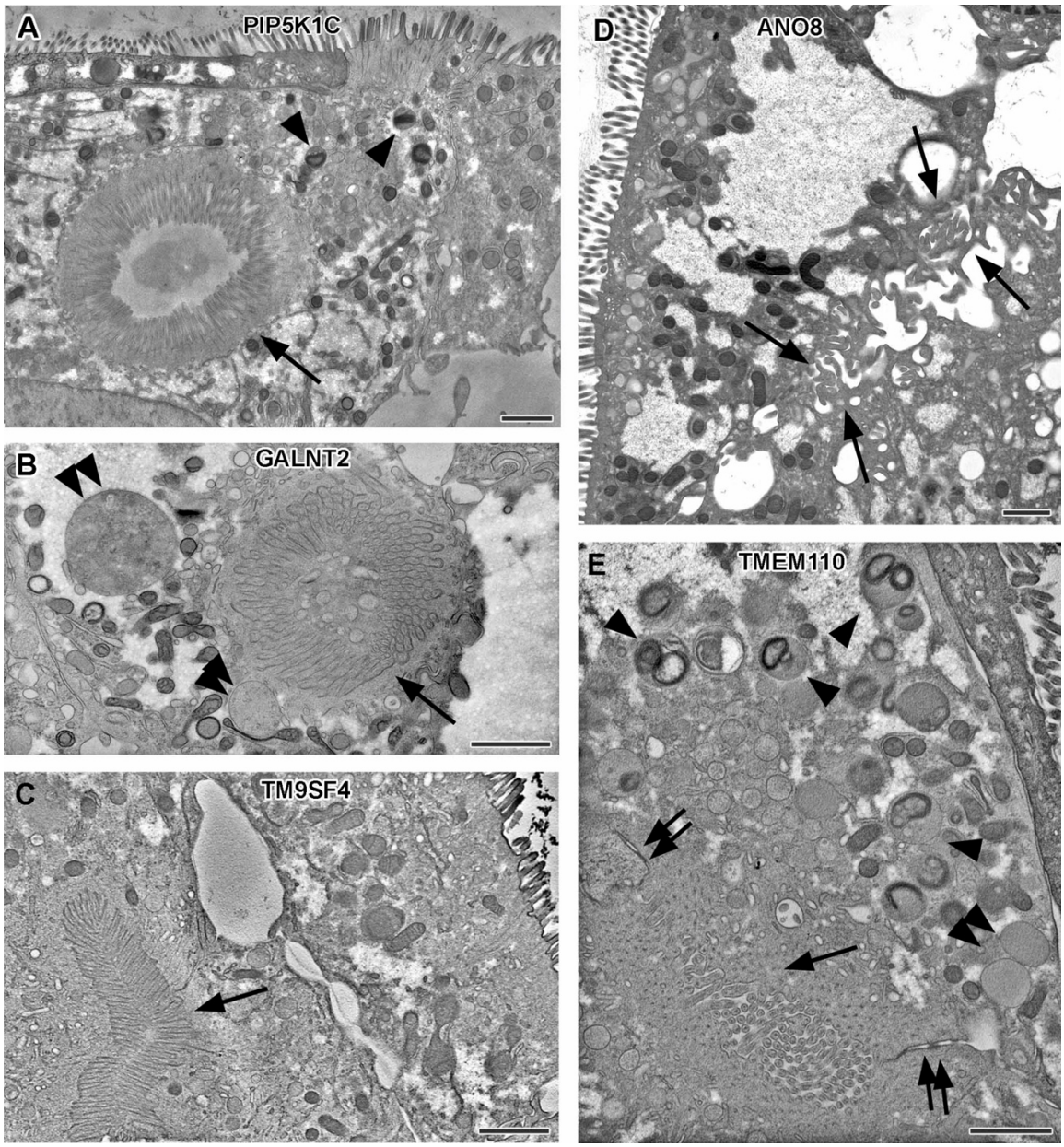

Figure 4. Electron micrographs with various configurations of abundant ectopic microvilli reflect polarity defects in 18-day-old 2D cultures of selected CaCo2 knock-down (KD) cell lines. Scale = 1 µm. A. Distinct intracellular lumen, lined by ectopic brush border and adjacent terminal web, thus, a typical microvillus inclusion (arrow) inside a PIP5K1C-KD cell. Arrow-heads mark lysosomes. **B.** Spherical intracellular mass of tangled microvilli associated with ectopic terminal web (arrow) inside a GALNT2-KD cell. Double arrow-heads mark enlarged late endocytic organelles. **C.** Paracellular, basolateral spot of densely packed microvilli plus associated ectopic terminal web (arrow) in polarized TM9SF4-KD-cell culture. **D.** Numerous, slightly bent microvilli facing widened intercellular space (arrows) in polarized ANO8-KD cell culture. **E.** Paracellular microvillar spot with adjacent ectopic terminal web (arrow) and associated cell junctions (double arrows) in polarized TMEM110-KD cell culture. Arrow-heads mark lysosomes, double arrow head marks a poorly structured late endocytic organelle.

In contrast to CaCo2 WT cells, all KD-cell lines had conspicuous clusters of ectopic microvilli (Fig. 4 A-E, Fig. S1 A, B). They appeared either as well-organized ectopic brush border and adjacent ectopic terminal web, lining distinct intracellular lumina (i.e., typical microvillus inclusions) (Fig. 4 A) or as less complex inclusions filled with intertwined masses of long, curved microvilli (Fig. 4 B, Fig. S1 B). Similar configurations occurred basolaterally as paracellular spots lined by densely packed microvilli (Fig. 4 C, E), frequently associated with ectopic tight- and adherens-junctions (Fig. 4 E). In addition, numerous long, curved microvilli were found facing the basolateral intercellular space (Fig. 4 D, Fig. S1 A), often forming conspicuous cell interdigitations. All these patterns together confirm the highly disturbed polarity of all KD cell lines studied here.

Notably, remarkable ultrastructural alterations also involved late endocytic and catabolic organelles (Fig. 5). In WT CaCo2 cells the different types and/or maturation stages of multivesicular bodies (MVBs) and lysosomes, as well as some autophagic organelles, appeared normal in size, abundance and morphology (Fig. 5 A and B) and resembled patterns previously mapped for other cryo-fixed mammalian cell lines (e.g., MEF, HeLa: (Vogel et al., 2015a; Yordanov et al., 2019; Hess and Huber, 2021)). However, in all KD-lines, the late endosomal/lysosomal endomembrane system was dominated by partly huge, spherical organelles (in addition to normal MVBs) − at the expense of normal lysosomes (Fig. 4 B and E; Fig. 5 C-G: double arrow-heads). These large compartments had either weakly stained, homogeneous granular contents with few intraluminal elements (Fig. 4 B and E; Fig. 5 C-G), or different amounts of partially degraded material. According to ultrastructural criteria, we tentatively interpreted these poorly structured, faint compartments as types of peculiar endolysosomes or (autophago)lysosomes (Bright et al., 2016; Fujita et al., 1990; Remis et al., 2014). Their size and frequency varied throughout the different KD-lines. Especially in TM9SF4-, ANO8- and ARHGAP33-KD they reached dimensions of up to 2x6 µm in diameter (e.g., Fig. 5 C), in other KD cell lines only diameters of approx. 500nm. In CaCo2 WT cells we sporadically found this type of organelle as well, but here they had rather normal dimensions (Fig. 5 A and B: double arrow-heads).

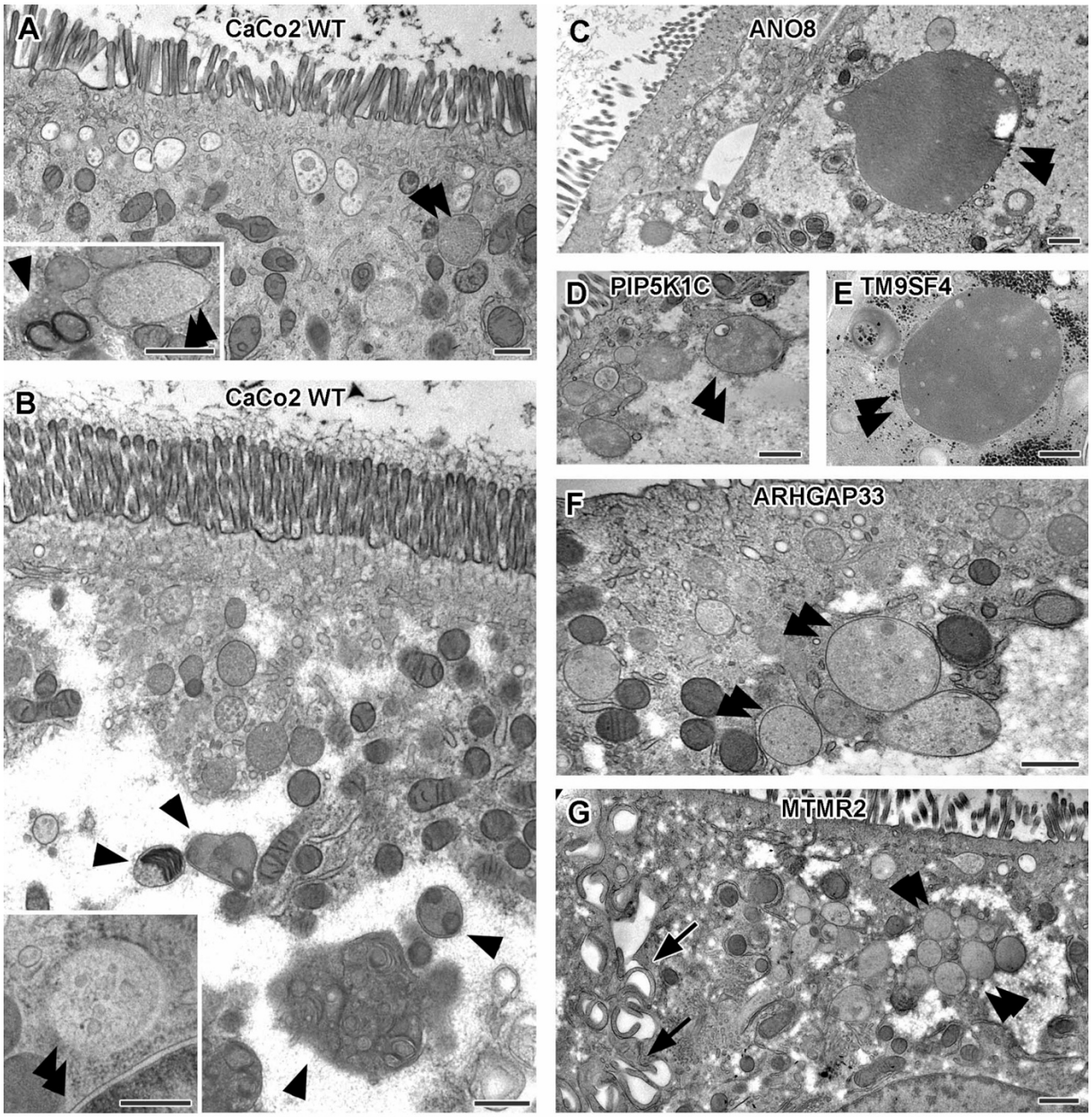

Figure 5. Ultrastructure of late endocytic and lysosomal organelles in CaCo2 wildtype (WT) cells versus selected knock-down (KD) cell linesof cryo-fixed 18-day-old polarized filter cultures under steady state conditions. Scale = 500 nm. A,B. WT CaCo2 cells with normal endosomes and lysosomes: multi-vesicular bodies (MVBs) with varying contents (regarding intraluminal vesicle (ILV) number, size and staining patterns), different types of (autophago)lysosomes (arrow-heads), all filled with clearly stained, finely granular material plus membrane remnants (i.e., multilamellar bodies) and/or opaque, amorphous residues (i.e., dense-core lysosomes). Double arrow-heads mark rare examples of inconspicuous spherical organelles with weakly stained, quite homogeneous granular contents harboring only sporadic ILVs and/or other structured components, interpreted as kind of endolysosome (Bright et al., 2016). **C.** Large, poorly structured putative endolysosome (double arrow-head), practically the only type of late endocytic and/or catabolic organelles in ANO8 KD under steady state. **D.**

Moderately sized and slightly enlarged putative endolysosomes (double arrow heads) occurring together with normal lysosomes in PIP5K1C KD cells. **E.** Enlarged putative endolysosome (arrow-head), the predominant type of late endocytic/catabolic organelles in TM9SF4 KD cells. **F.** Moderately enlarged putative endolysosomes (double arrow heads) occurring together with a few normal lysosomes in ARHGAP33 KD cells. **G.** Moderately enlarged putative endolysosomes (double arrow heads) occurring together with a few normal lysosomes in MTMR2 KD cells. Arrows mark lateral microvilli.

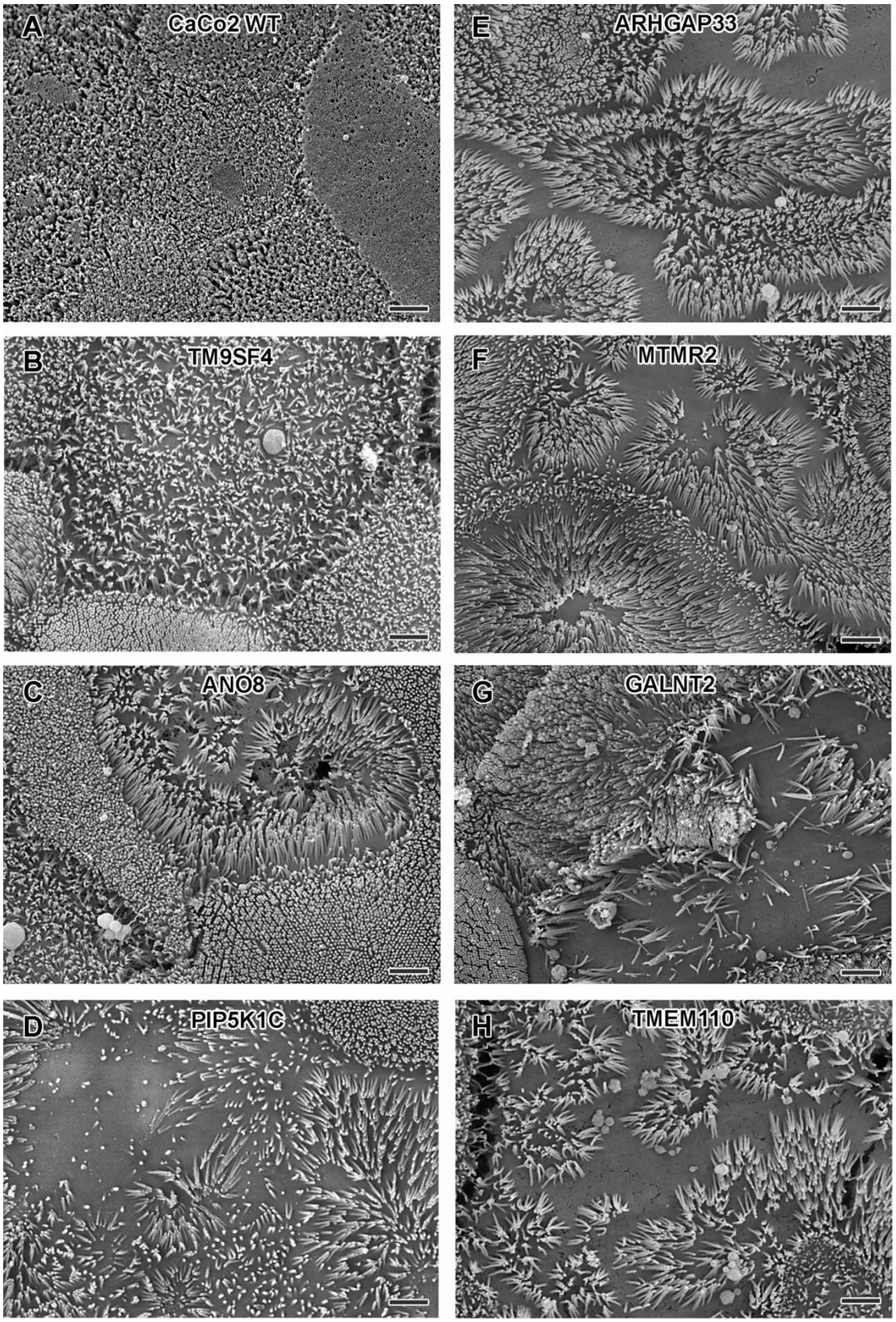

Figure 6. Scanning EM surface views on apical microvilli of 18 day-old polarized CaCo2 wildtype (WT) cells versus knock-down (KD) cells. Scale = 2 µm. A. CaCo2 WT cells with dense, quite uniform brush border. **B-H.** Patchy distribution of partly abnormal microvilli characterize the apical surface of all KD cell lines specified here.

Regarding the general architecture of the brush border, scanning electron microscopy (SEM) and actin fluorescence microscopy revealed more or less severe irregularities in in all KD-cell lines studied here (Fig. 6-9). They included patchy distribution or complete absence of apical microvilli, together with the occurrence of extremely long microvilli (Fig. 6 B to H). We then combined actin labeling with immunofluorescence microscopy using antibodies against the apical components DPP4 and stx3 (Fig. 7 A-D; Fig. 8 A-D; Fig. 9 A-H). At first glance, we detected DPP4 in most CaCo2-KD monolayers predominantly at the apical plasma membrane. However, more detailed analysis of confocal stacks revealed that DPP4 was also mislocalized to intracellular structures in ARHGAP33-, TM9SF4-, PIP5K1C-, MTMR2- and ANO8-KD-cell lines (Fig. 7 B-D; Fig. 9 A and B), although to varying degrees. While DPP4 was mislocalized to subapical compartments in ARHGAP33-, TM9SF4- and ANO8-KD cell lines, PIP5K1C- and MTMR2-KDs displayed DPP4 localization to large, actin-rich, basolateral structures, reminiscent of microvillus inclusions, observed by EM. Consistent with these observations, stx3 was detected at the apical brush-border microvilli in all KD cell lines (Fig. 8 B-D; Fig. 9 E-H). However, this was accompanied by additional ectopic localization of stx3 in TM9SF4-, ARHGAP33-, MTMR2- and PIP5K1C-KDs, with MTMR2- and PIP5K1C-KDs exhibiting stx3-positive, basolateral inclusion-like compartments (Fig. 8 D and Fig. 9 F), whereas stx3-positive structures were seen in apical regions in TM9SF4- and ARHGAP33-KD cells (Fig. 8 B and Fig. 9 E). To investigate whether KD of each candidate also affects the junctions and differentiation of basolateral domains, we stained all cell lines for the apical tight-junction protein claudin-3, and the basolateral adherens junction protein E-Cadherin (Fig. 10 A-H). Our analyses revealed a generally normal distribution of those markers in all KD-cell lines. Claudin-3 showed the characteristic localization pattern, with an enrichment towards the apical domain and locally also lateral membrane distribution and E-Cadherin marking basolateral membrane domains (Fig. 10 A-H). Interestingly, transepithelial electric resistance (TEER) measurements of filter-grown, polarized 2D monolayers of WT and KD-cell lines revealed an increase of TEER after measurement-day 7 upon KD of ARHGAP33, while TEER of the other KD-cell lines remained comparable to those of WT cells (Fig. 10 I).

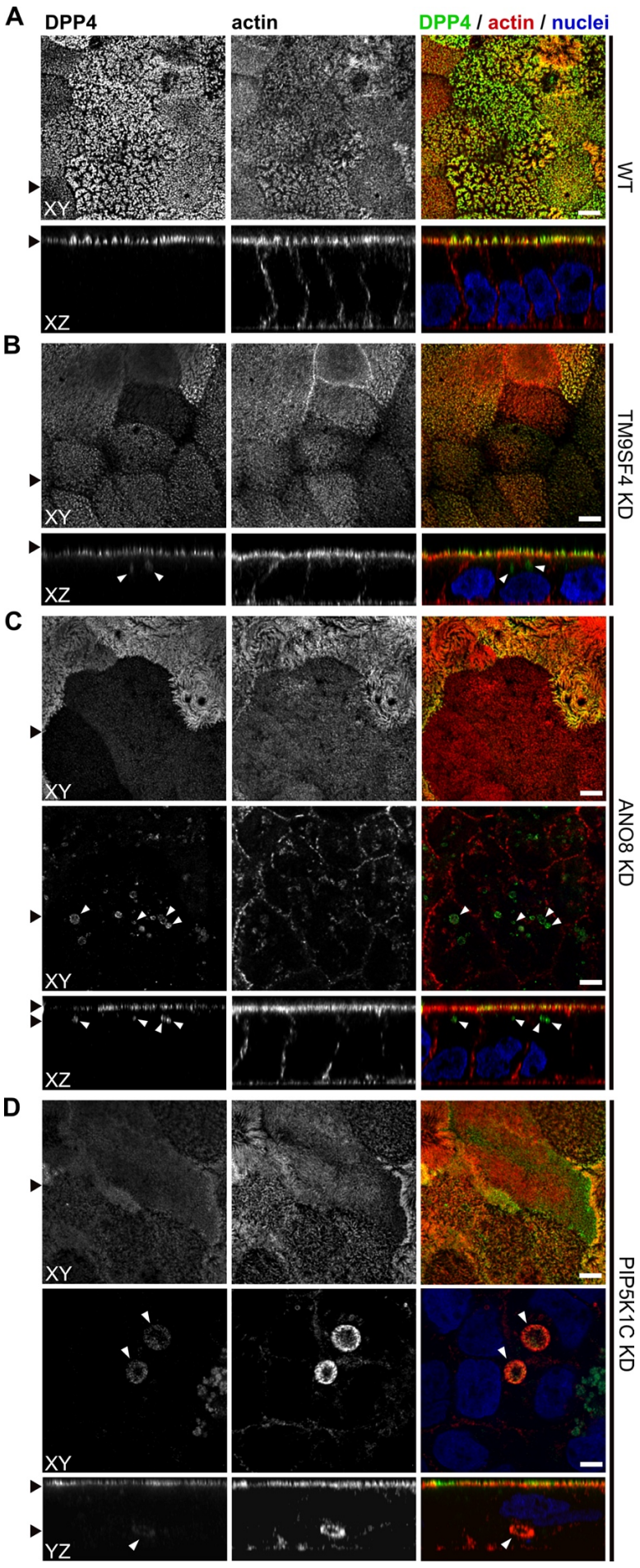

Figure 7. Confocal micrographs of DPP4 and actin immunofluorescence staining from wildtype (WT) and respective knock-down (KD) cell lines. A. DPP4 localization is restricted to the actin-rich microvillus brush-border in WT cells. **B, C.** DPP4 can still be targeted to the apical plasma membrane, but also mislocalizes to subapical compartments in TM9SF4- (B) and ANO8-KD (C) cells (white arrowheads). **D.** PIP5K1C-KD cell lines display large, DPP4- and actin-positive, basolateral compartments (white arrowheads). XY = top view of polarized monolayer; XZ/YZ = lateral view of polarized monolayer. Scale = 5µm.

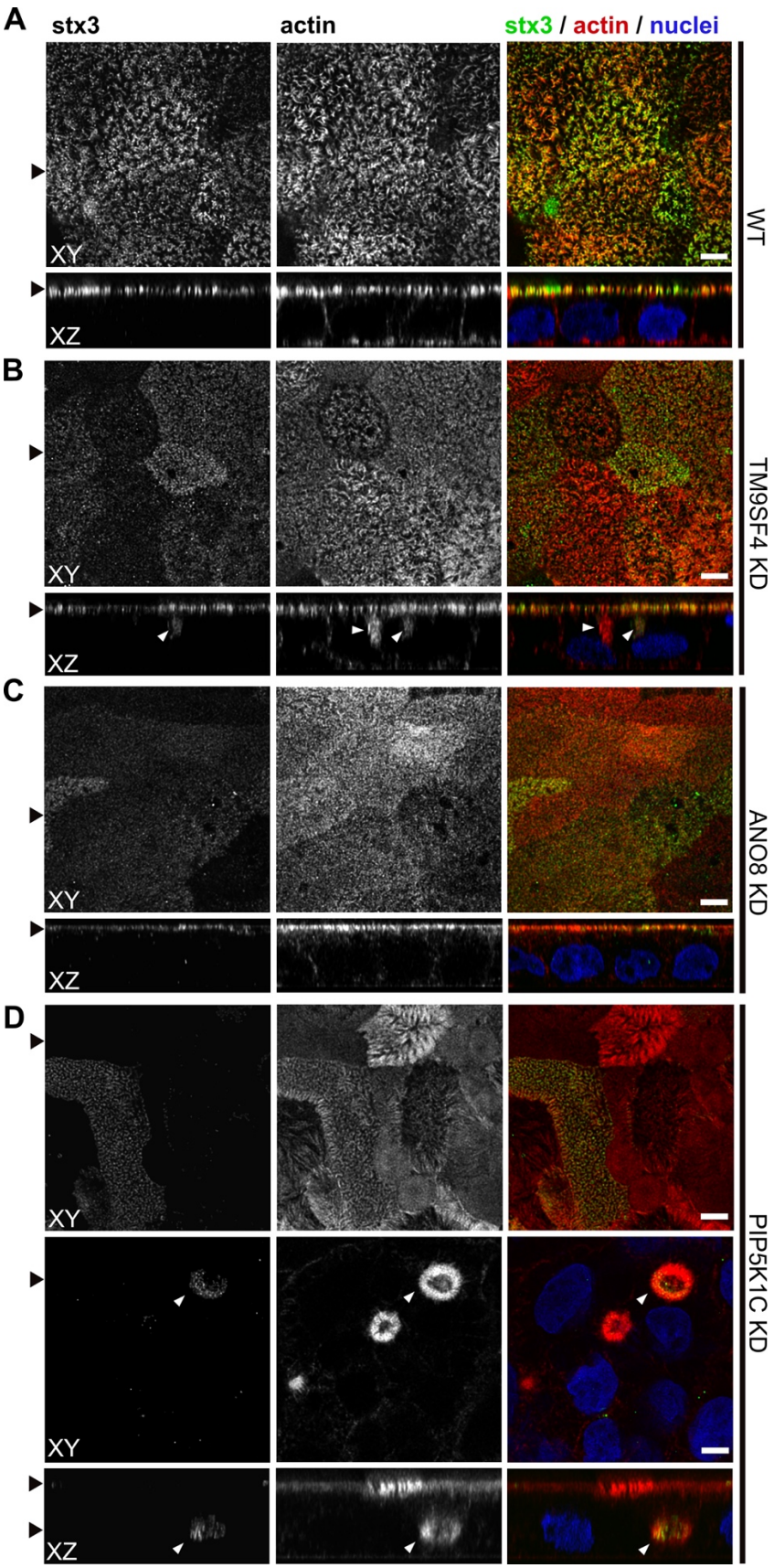

Figure 8. Confocal micrographs of syntaxin-3 (stx3) and actin immunofluorescence staining from wildtype (WT) and respective knock-down (KD) cell lines. A. stx3 localizes strictly to the apical plasma membrane in WT cells. **B.** stx3 abberantly localizes to a subapical

409 compartment in TM9SF4-KD cells. **C.** ANO8-KD cell lines display apical localization of stx3. **D.**
410 stx3 mislocalizes to large, basolateral, actin-rich compartments in PIP5K1C-KD cells,
411 reminiscent of microvillus inclusions. XY = top view of polarized monolayer; XZ/YZ = lateral
412 view of polarized monolayer. Scale = 5μm.

413

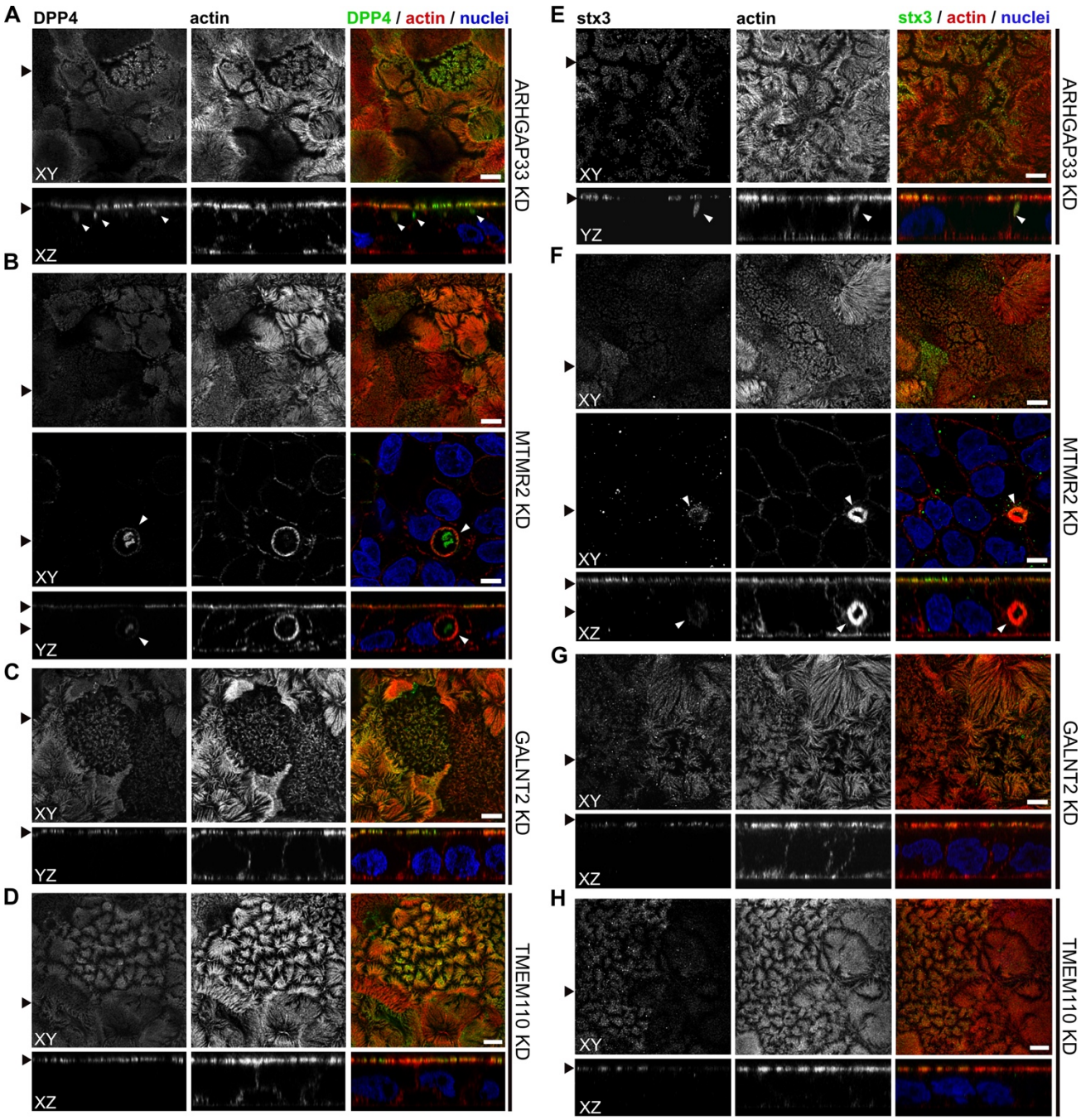

414

415 **Figure 9. Confocal micrographs of DPP4 (A-D) and stx3 (E-H) together with actin**
416 **immunofluorescence staining of knock-down (KD) cell lines. A.** DPP4 mislocalizes to
417 subapical compartments in ARHGAP33-KD cells (white arrowheads). **B.** MTMR2-KD cell lines
418 display large, actin rich basolateral compartments, that also show DPP4 (white arrowheads). **C-**
419 **D.** In GALNT2- and TMEM110-KD cells, DPP4 localizes strictly to the apical plasma membrane.

E. stx3 localizes to a subapical compartment in ARHGAP33-KD cells. **F.** stx3 mislocalizes to large, basolateral actin-rich compartments in MTMR2-KD cells. **G-H.** GALNT2- and TMEM110-KD cell lines display apical localization of stx3. XY = top view of polarized monolayer; XZ/YZ = lateral view of polarized monolayer. Scale = 5μm.

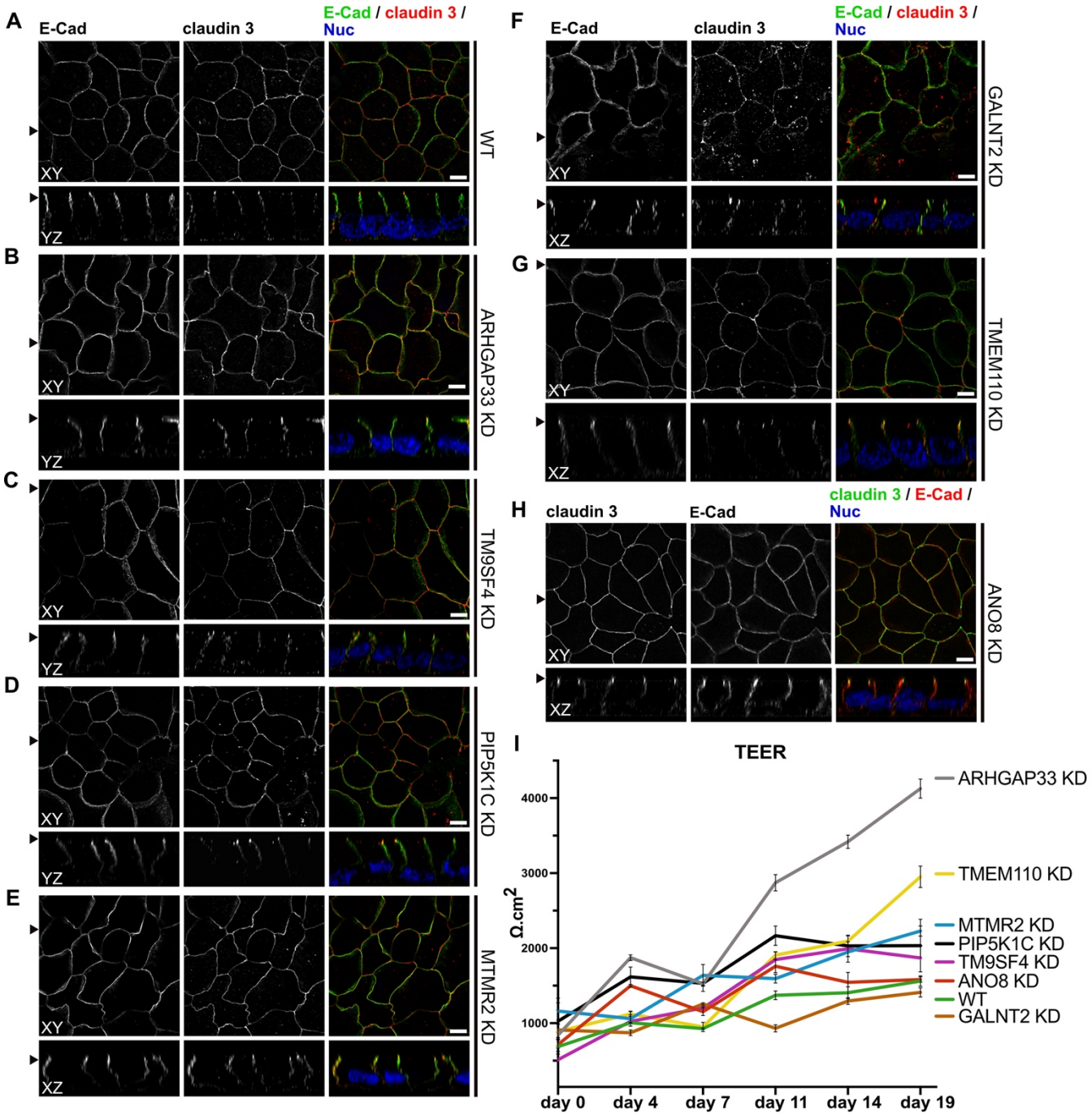

Figure 10. Confocal micrographs of E-Cadherin and claudin 3 immunofluorescence staining from wildtype (WT) and respective knock-down (KD) cell lines. A. Localization of E-Cadherin and claudin 3 in WT cells, where E-Cadherin is distributed over the basolateral plasma membrane and claudin 3 is enriched at apical domains, but can also be found at

basolateral membrane regions. **B-H.** ARHGAP33-, TM9SF4-, PIP5K1C-, MTMR2-, GALNT2-, TMEM110- and ANO8-KD cell lines show basolateral E-Cadherin localization as well as claudin 3 enrichment at apical and lateral domains, similar to WT cells (A). Scale = 5 µm. **I.** TEER-measurements of WT and respective KD clones. TEER of ARHGAP33-KD cells increases substantially around day 7 of the measurement. Measurements are depicted as means with standard-deviation. XY= top view of polarized monolayer; XZ/YZ= lateral view of polarized monolayer

Taken together, our analyses have so far provided several indications of polarity defects after elimination of the selected candidates (Table 1): In a 3D-polarization assay, all KD-cell lines showed severe defects in forming normal cysts with a single, central lumen but rather generated multiple lumina or no lumina at all. Additionally, TM9SF4-, ANO8- and MTMR2-KD-cell lines showed intracellular mislocalization of the apical marker DPP4 in 3D cysts. Transmission EM of polarized 2D monolayers revealed that KD of all candidates induced ectopic intra- and paracellular clusters of microvilli, reminiscent of typical microvillus inclusions, and SEM complemented these findings with observed alterations in apical brush-border formation in all generated KD cell lines. Immunofluorescence micrographs finally confirmed these observations and additionally indicated partial mislocalization of apical proteins (Fig. 13 B).

Apical markers mislocalize in enlarged, degradative compartments of TM9SF4-, ARHGAP33- and ANO8-KD cells

To further complement these results, we used single and double immunogold labeling primarily to characterize the abnormally large, usually poorly structured organelles in TM9SF4, ANO8, and ARHGAP33 KDs and to evaluate their possible association with the abnormal intracellular DPP4 staining in immunofluorescence (Fig. 11 A-G). Membrane or contents of those compartments showed distinct Lamp1, Lamp3 or CathepsinD immunogold label, respectively, in all 3 KD-cell lines (Fig. 11 A, C and D). These findings were also consistent with Lamp1 immunofluorescence micrographs (Fig. 12 A-D). Successful immunogold detection of the previously internalized acidotropic reagent DAMP provided further evidence for the clearly acidic nature of those organelles, justifying their classification as species of modified endolysosomes/(autophago)lysosomes (Fig. 11 B, Fig. S1 C and D). They regularly contained mislocalized DPP4 (Fig. 11 C and D; Fig. S1 C, D). Moderate, but distinct, aberrant stx3 label that was not detectable by immunofluorescence was also observed in these organelles − in addition to normal apical localization and ectopic localization of stx3 and DPP4 at microvillus inclusions and paracellular microvillar spots (Fig. S1 I and J). Further insight into the late

endocytic/catabolic endomembrane system of TM9SF4-, ANO8- and ARHGAP33-KD cells was obtained from starvation experiments. After serum deprivation overnight almost all the giant, poorly structured, faint compartments had disappeared, likely due to autophagic removal, and reformed lysosomes of normal size and morphology were regularly observed (Fig. S1 E-H).

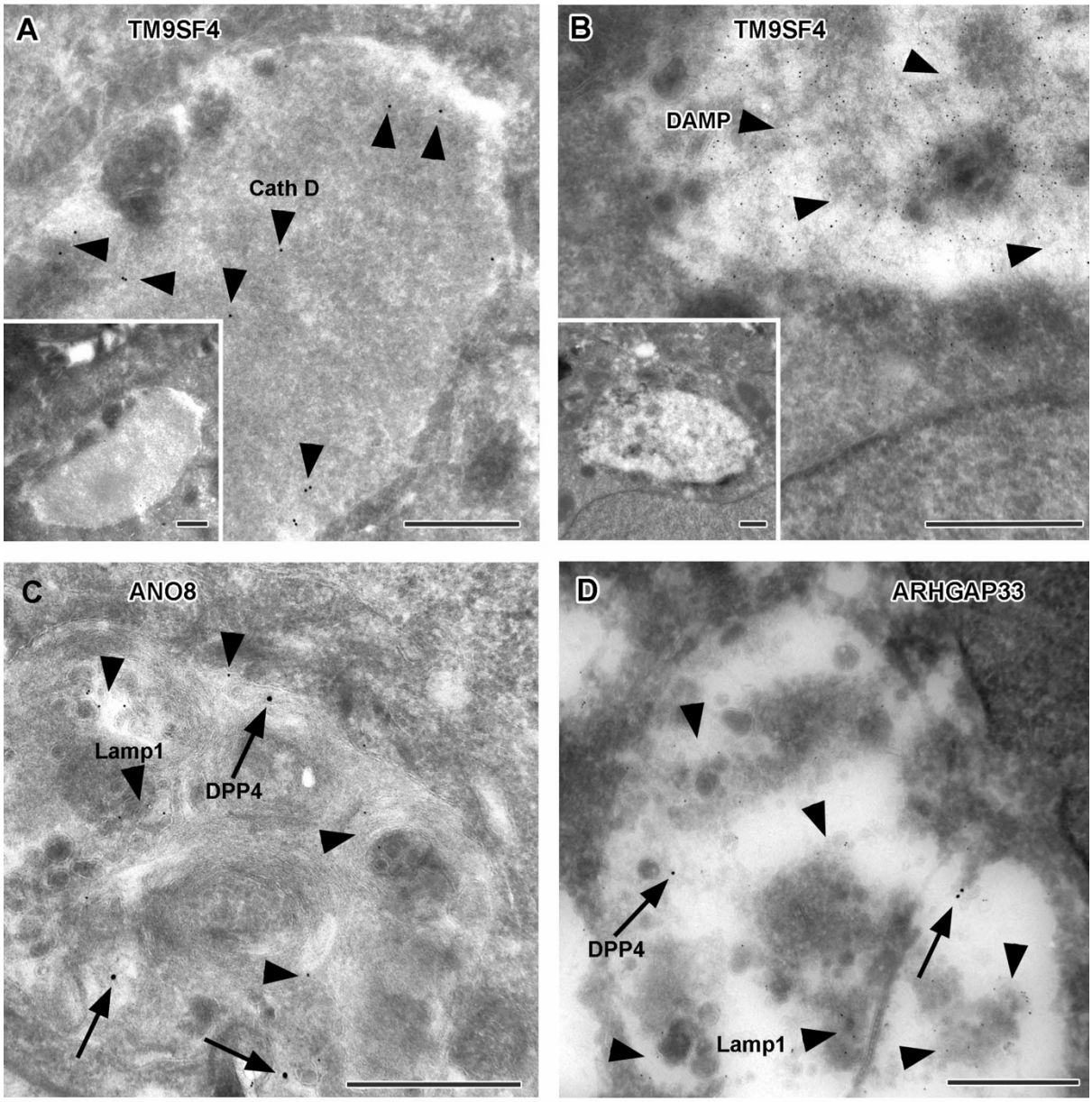

Figure 11. Immunoelectron microscopy of late endocytic and catabolic organelles in selected CaCo2 knock-down (KD) cells. Scale = 500 nm. A,B. Enlarged, poorly structured endolysosomes in TM9SF4 KD cells showing distinct cathepsin D and DAMP-immunogold label (arrow heads) indicative of their acidic contents. Inserts show respective overviews of the depicted organelles. **C,D.** Mislocalized DPP4 (arrows) colocalizing with LAMP1 (arrow heads) in enlarged compartments in ANO8 and ARHGAP33-KD cells.

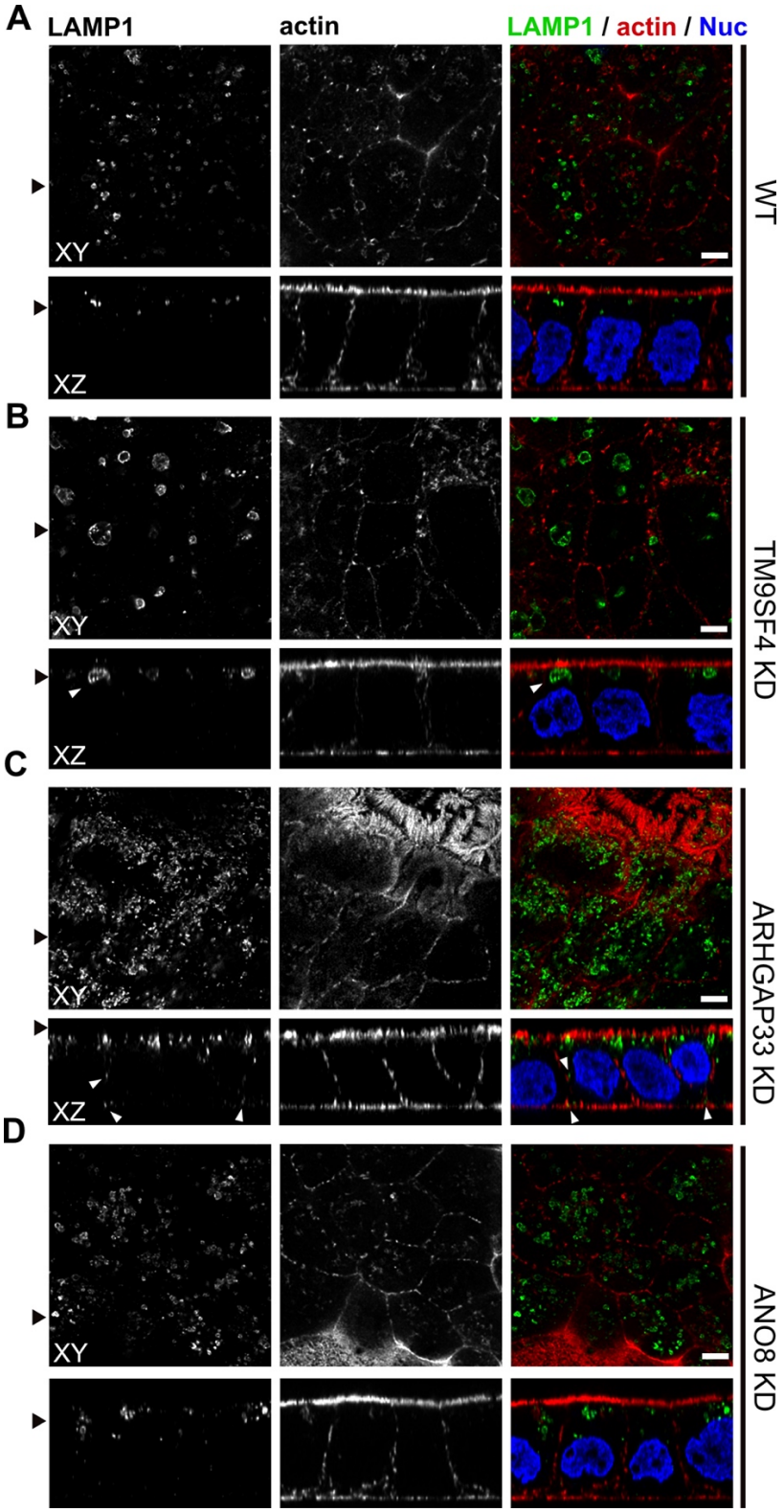

Figure 12. Confocal micrographs of Lamp1 immunofluorescence staining from wildtype (WT) and respective knock-down (KD) cell lines. A-D. The Lamp1-positive compartments appear enlarged upon KD of TM9SF4 (**B**) and localize to basolateral regions upon KD of ARHGAP33 (**C**) (white arrowheads). Scale = 5 µm.

Finally, ZO-1 and E-cadherin immunogold labeling allowed us to verify our ultrastructural observations of ectopic tight and adherens junctions associated with paracellular clusters of microvilli, that were not seen in lower resolution immunofluorescence micrographs (Fig. S1 K and L).

In summary, our analyses showed that in addition to defects in cell polarization, KDs of all candidates lead to basolateral mislocalization of apical cargo (Table 1). In particular, we observed localization of DPP4 and stx3, to enlarged, endolysomal/lysosomal compartments, as shown by immunogold labeling of Lamp1, Lamp3, and CathepsinD (Fig. 13 B; Table 1). Moreover, these enlarged compartments were always capable of acidification, and apparently also autophagic degradation and lysosomal reformation. Thus, our observations suggest that KD of the factors studied, TM9SF4, ANO8 and ARHGAP33, leads to aberrant traffic of apical cargo proteins.

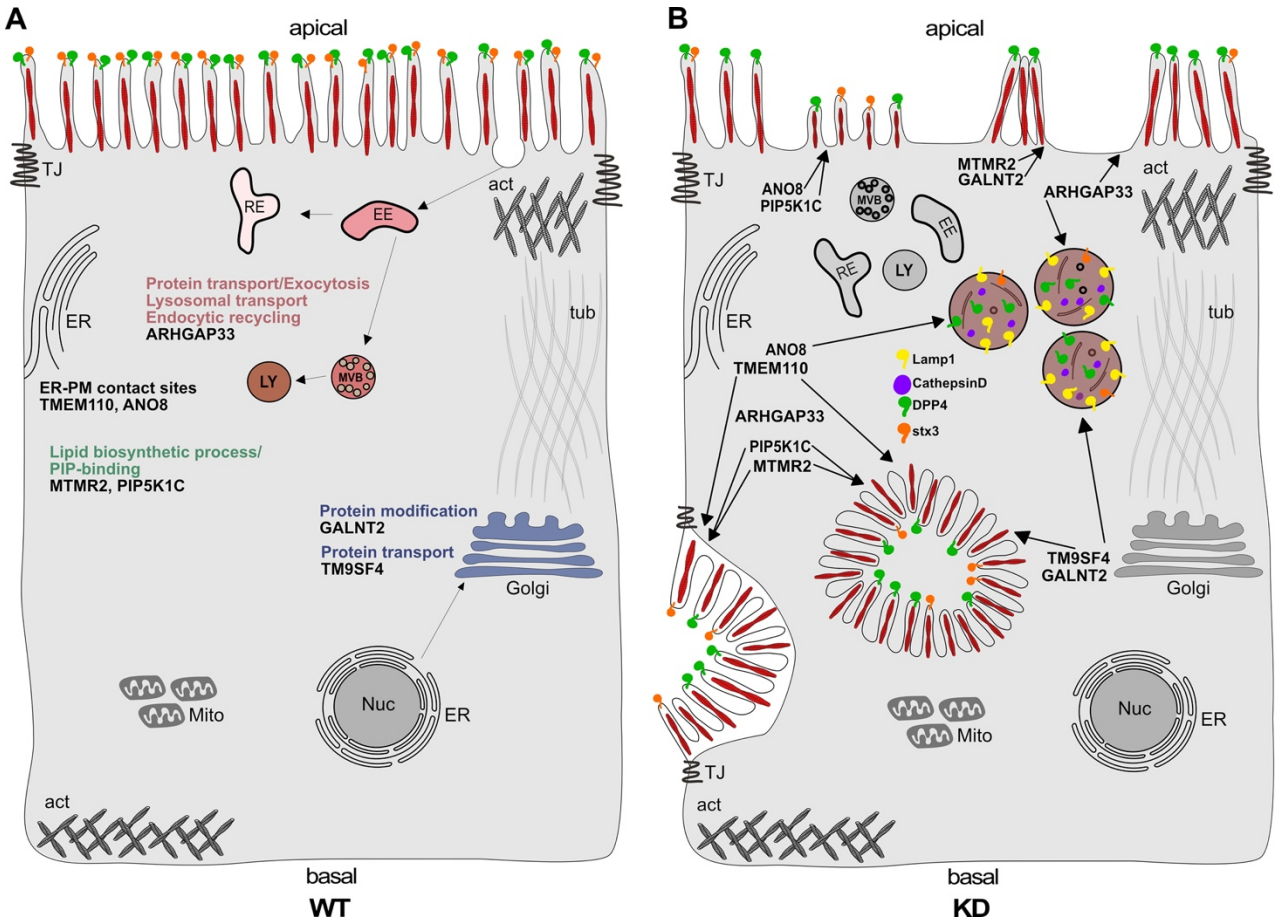

Figure 13. Simplified scheme of the phenotypes observed upon knock-down (KD) of ARHGAP33, TM9SF4, PIP5K1C, MTMR2, GALNT2, ANO8 and TMEM110. A. Scheme of a healthy enterocyte. The investigated factors for screen validation and further phenotypic characterization are displayed together with their associated GO-terms. **B.** KDs of ARHGAP33, TM9SF4, PIP5K1C, MTMR2, GALNT2, ANO8 and TMEM110 lead to the formation of

microvillus inclusions and lateral pseudo-apical domains with microvilli. KD of ARHGAP33, TM9SF4 and ANO8 leads to the formation of enlarged late endosomal/lysosomal compartments positive for Lamp1 and Cathepsin-D and that contain the apical markers DPP4 and stx3. All KDs additionally lead to aberrant, “tipi-like” assemblies of apical microvilli.

Table 1. Synopsis of phenotype characteristics of CaCo-WT versus TM9SF4-, ANO8-, PIP5K1C-, ARHGAP333-, MTMR2-, TMEM110-KD cells

Phenotype characteristics of CaCo-WT *versus* TM9SF4-, ANO8-, PIP5K1C-, ARHGAP333-, MTMR2-, TMEM110-KD cells

		CaCo2-WT	TM9SF4-KD	ANO8-KD	PIP5K1C-KD	ARHGAP33-KD	MTMR2-KD	GALNT2-KD	TMEM110-KD
FACS	**DPP4 intensity**	100%	50%	70%	25%	70%	70%	50%	50%
IF: 3D	**Cyst lumen**	single	multiple	multiple	multiple	multiple	multiple	multiple	multiple
IF: 3D	**DPP4**	Brush border (BB)	BB, intracellular dots	BB, intracellular dots	BB	BB	BB	BB, intracellular dots	BB
IF: 2D	**DPP4**	BB	BB, subapical dots	BB, subapical dots	BB, basolateral MVI/par MV	BB, subapical dots	BB, basolateral MVI/par MV	BB	BB
IF: 2D	**stx3**	BB	BB, subapical dots	BB	BB, basolateral MVI/par MV	BB, subapical dots	BB, basolateral MVI/par MV	BB	BB
IF: 2D	**LAMP1**	normal subapical organelles	huge subapical organelles	large subapical organelles	*n.d.*	subapical & basolateral organelles	*n.d.*	*n.d.*	*n.d.*
SEM: 2D	**Apical microvilli**	dense BB, uniform	± patchy BB, partly irregular size/shape	± patchy BB, partly irregular size/shape	± patchy BB, partly irregular size/shape	± patchy BB, partly irregular size/shape	± patchy BB, partly irregular size/shape	± patchy BB, partly irregular size/shape	± patchy BB, partly irregular size/shape
TEM: 2D	**Ectopic microvilli**	negligible	MVI, par MV, lat MV	MVI, par MV, lat MV	MVI, par MV, lat MV	MVI, par MV, lat MV	MVI, par MV, lat MV	MVI, par MV, lat MV	MVI, par MV, lat MV
IEM: 2D	**Ectopic junctions: ZO-1, E-cadherin**	*n.d.*	par MV	par MV	*n.d.*	par MV	*n.d.*	*n.d.*	*n.d.*
TEM: 2D	**Lysosomes (LY)**	typical, predominant	typical, very rare	typical, very rare	typical, frequent	typical, rare	typical, moderate	typical, predominant	typical, predominant
TEM: 2D	**Endolysosomes (ELY)**	normal-sized, rare; Lamp1 & 3, CathD, DAMP	huge, abundant; Lamp1 & 3, CathD, DAMP	huge, abundant; Lamp1 & 3, CathD, DAMP	enlarged, frequent; *IEM: n.d.*	enlarged, frequent; Lamp1 & 3, CathD, DAMP	enlarged, frequent; *IEM: n.d.*	normal-sized, moderate; *IEM: n.d.*	normal-sized, moderate; *IEM: n.d.*
IEM: 2D	**DPP4**	BB	BB, ELY, MVI, par MV	BB, ELY, MVI, par MV	*n.d.*	BB, ELY, MVI, par MV	*n.d.*	*n.d.*	*n.d*
IEM: 2D	**stx3**	BB	BB, MVI, par MV (ELY)	BB, MVI, par MV (ELY)	*n.d.*	BB, MVI, par MV (ELY)	*n.d.*	*n.d.*	*n.d.*

Abbreviations: BB= brush border, CathD=Cathepsin D, ELY=endolysosomes, LY=lysosomes, MVI=microvillus inclusions, lat MV= lateral microvillar assemblies, par MV=paracellular microvillar clusters, n.d.=not done, IEM=immuno-EM, SEM=Scanning EM, TEM=Transmission EM

Discussion

Coordination of molecular polarization and transport machineries in concert with polarized cargo sorting mechanisms is key to epithelial tissue homeostasis. Numerous studies have contributed to our understanding of these processes in the past (Bryant et al., 2010; Levic and Bagnat, 2021; Apodaca et al., 2012). Our previous findings on the mechanisms underlying MVID have elucidated the role of a myo5b-stx3-munc-18-2-dependent trafficking cascade for apical, actin-based cargo delivery; they also suggest the presence of additional trafficking routes and transport mechanisms that direct protein secretion to the apical cortex (Vogel et al., 2015b, 2017a; b), which have not been elucidated to date. However, technical advances in CRISPR-technology, particularly the development of CRISPR-screening strategies, have paved the way for the discovery of protein functions for a wide range of cellular processes (Popa et al., 2020; Hutter et al., 2020; Zhu et al., 2021). In particular, CRISPR-mediated loss of function screens have proven to be highly efficient in discovering novel factors for intracellular protein transport and secretory trafficking (Stewart et al., 2017; Bassaganyas et al., 2019).

Here we performed the first CRISPR-Cas9 loss of function screen in polarized human epithelial cells to identify novel regulators of epithelial polarization and polarized membrane trafficking. We developed a FACS-based assay for the detection of endogenous plasma membrane cargo, which is easy to apply and can be adapted to a variety of transmembrane proteins, given that specific antibodies are available. For our purposes, we used this assay in combination with the highly efficient CRISPR screening system to study genes involved in plasma membrane targeting of the apical model cargo DPP4. Furthermore, it seems obvious and feasible to adapt this FACS-based assay for other types of apical transmembrane cargo, thus expanding the range of data that can be obtained with whole-genome screenings. Our CRISPR-screen in polarized enterocytes identified 89 genes, critically involved in apical targeting of our model cargo, DPP4. This rather moderate number of enriched genes resulted from the high stringency in the screening assay, namely sorting for cells with a quite drastic reduction of surface DPP4 (90%). Even though this allowed to enrich for cells with a high gRNA targeting efficiency and increased the specificity of our screen, we thereby also limited our approach in terms of quantity and diversity of the identified hits.

Our experimental approach, combined with GO analysis of the 89 hits, highlighted several genes with functions associated to the secretory pathway. To demonstrate the validity of our dataset, we selected 7 factors for phenotypic and morphological characterization, focusing, mainly on organelles associated with protein transport.

We demonstrated that KD of all selected candidates causes disturbed epithelial polarization. This was demonstrated by 3D cyst assays and EM analyses of filter-grown, polarized 2D

559 monolayers, where we detected the formation of ectopic, intracellular and paracellular clusters
560 of microvilli. This phenotype was particularly pronounced in KD cells of PIP5K1C and MTMR2,
561 where the localization of the apical components DPP4, stx3 but also ZO-1 in the intracellular
562 and paracellular microvillar clusters indicated the formation of ectopic neo-/pseudo-apical
563 domains. This highlights yet uncharacterized regulators for epithelial polarization and proposes
564 potentially novel mechanisms for this process. PIP5K1C and MTMR2 are involved in the
565 regulation of PIP-pools accounting for apical PM composition and hence we propose
566 imbalances in cellular PIP-pools as basis for the observed phenotypes. Interestingly, MTMR2
567 and PIP5K1C mRNAs were shown to be expressed mostly in polarized 2D-cultures, and are
568 downregulated in 3D cysts of MDCK cells, suggesting differential PIP-regulation in 2D
569 polarized monolayers and polarization 'de-novo' (Román-Fernández et al., 2018). In contrast,
570 our data suggests a role for both enzymes in polarization of 3D cultures as well, as we observe
571 aberrant lumen formation upon KDs.

572 Furthermore, the diversity of signals and determinants that coordinate the formation of
573 specialized membrane domains is illustrated by the different functions with which the
574 candidates selected here are associated. The ER-PM contact site proteins ANO8 and
575 TMEM110 might regulate polarization via the control of Ca2+ influx and signaling (Jha et al.,
576 2019; Quintana et al., 2015), while TM9SF4, which has been implicated in the regulation of
577 glycolipids in the Golgi apparatus (Perrin et al., 2015) and VH-ATPase assembly (Lozupone
578 et al., 2015), possibly controls polarization through generation of lipid microdomains and pH-
579 regulation. GALNT2 might contribute to establishing polarity via its role as O-glycosylating
580 enzyme in the Golgi apparatus and ARHGAP33, as a GAP-protein for the small GTPase
581 Cdc42, might itself be critically involved in polarization and polarized traffic as well (Nakazawa
582 et al., 2016). Here, elevated TEER-levels upon KD of ARHGAP33 are further evidence of
583 fundamentally disturbed epithelial polarity, supporting this hypothesis.

584 Features indicating disturbed polarization, were accompanied by the formation of conspicuous,
585 enlarged Lamp1, Lamp3 and Cathepsin-D-positive endolysomal/lysosomal structures, upon
586 KD of all cell lines, that were additionally positive for DPP4 and stx3 in ANO8-, ARHGAP33-
587 and TM9SF4-KDs. Notably, these compartments showed functional acidification and could
588 undergo autophagic degradation followed by lysosomal reformation. Therefore, we propose
589 that defective polarization upon disruption of one of these genes may be associated with
590 altered cargo transport and/or sorting of apical cargo into lysosomal compartments by various
591 cellular mechanisms. Little is known about a potential role for ARHGAP33 in epithelial
592 polarization, however, it is arguable that a role in modulating Cdc42 might account for the
593 observed polarity defect and the mislocalization/mistrafficking of apical cargo to late-
594 endosomes/lysosomes (Nakazawa et al., 2016; Schuster et al., 2015). The Golgi apparatus is
595 believed to be a major hub for sorting events of secreted cargo proteins and many signals and

mechanisms have been proposed to be major Golgi-associated sorting determinants (Weisz and Rodriguez-Boulan, 2009; Rodriguez-Boulan et al., 2005). Ca2+ levels in the Golgi apparatus, for example, were shown to regulate apical sorting of GPI-anchored proteins in polarized epithelial cells (Lebreton et al., 2021). Thus, mislocalization of DPP4 in ANO8-KDs to endosomal/lysosomal compartments could result from aberrant, Ca2+ dependent sorting in the Golgi apparatus. Finally, lipid microdomains and pH-regulation represent major sorting determinants of apical cargo in the Golgi (Hallermann, 2014; Medina et al., 2015; De Araujo et al., 2017; Schuck and Simons, 2004). Therefore, it is plausible to assume that the observed mistargeting of apical cargo into lysosomal compartments may coincide with defects in glycosphingolipid synthesis and/or V-ATPase-mediated pH-regulation, caused by TM9SF4-KD (Lozupone et al., 2015; Levic et al., 2020; Levic and Bagnat, 2021).

It seems noteworthy that cellular Ca2+ homeostasis, the regulation of intracellular pH, as well as the synthesis PIP-species and lipid microdomains regulate a variety of processes related to endocytic recycling of membrane cargo, autophagy, and lysosomal biogenesis (Medina et al., 2015; Sbano et al., 2017; Hallermann, 2014). Defects in either of these processes could therefore be responsible for the observed lysosome-related phenotypes, leading either primarily or secondarily to defective epithelial polarization/secretory traffic.

Taken together, our data suggests that the generation of specialized membrane domains and specialized membrane traffic are regulated by the interplay of several determinants of polarization, trafficking, and cargo sorting, such as the synthesis of PIP species and glycosphingolipids, N-/O-linked glycosylations, and changes in cellular Ca2+ levels or pH regulation.

Because several diseases characterized in the past have been associated with defects in polarized trafficking and protein missorting, we also screened our dataset for all possible genes that have been associated with congenital enteropathies. Apart from the association of Unc-45 Myosin Chaperone A (UNC45A) with syndromal diarrhea and cholestasis, no other genes identified in our CRISPR screen have been published in this context to date. (Esteve et al., 2018; Li et al., 2022; Dulcaux-Loras et al., 2022). However, MVID caused by mutations of myo5b, stx3, stxbp2, or unc45a is a prominent example for pathological accumulation of considerably enlarged autophagosomal and/or lysosomal organelles in the cell periphery. Despite their abundance, those catabolic organelles apparently suffer from some degree of overload due to their inability to remove misdirected excess cargo (i.e., "secretory granules") and efficiently degrade the ectopic apical domains/microvillar structures. Moreover, abnormal late endosomes/lysosomes with close resemblance to the respective faint, poorly structured lysosomal compartments in the phenotypes we describe here had recently also been implicated in another neonatal intestinal disorder, namely, human mucolipidosis type IV. In

newly born mice the absence of mucolipin-1 and 3 caused aberrant swelling of those organelles in enterocytes, diminished apical endocytosis from the intestinal lumen, diarrhea, and delayed growth (Remis et al., 2014). In our opinion, all those examples underline the crucial role of proper establishment and maturation of the highly complex system of (late) endosomal and lysosomal organelles in the small intestine, for example, during the early neonatal period of mammals, especially the transient, so-called "giant lysosomes" during the suckling period (Wilson et al., 1991; Fujita et al., 1990). In addition to neonates, this seemingly broad spectrum of overload and/or accumulation of enlarged catabolic organelles with enhanced - but insufficient - autophagy and lysosomal inefficiency has also been described from intestinal disorders of adults, e.g., in patients with necrotizing enterocolitis (Yamoto et al., 2020).

Finally, it should be noted that several genes identified in our screening have been associated with neuropathies or myopathies (Charcot-Marie-Tooth syndrome (MTMR2); Dyggve-Melchior-Clausen syndrome (DYM)) (Denais et al., 2011; Wang et al., 2019). Thus, it would be worthwhile to examine our dataset in the context of other cellular systems, as defective secretory transport and cellular polarization provide a mechanistic basis for a spectrum of pathologies in many tissues and organs.

In summary, this genome-wide CRIPR/Cas9 screen, together with the extensively described and illustrated representation of cellular organelle pathologies, provides a very valuable resource for future investigations aimed at unraveling the complexity and diversity of mechanisms underlying epithelial polarization and polarized cargo transport. In addition, this study can contribute to the understanding of many yet-to-be-discovered pathologies associated with impaired epithelial differentiation, polarization, and integrity and will therefore serve as a powerful resource for the investigation and characterization of congenital diseases. (Thiagarajah et al., 2018; Canani et al., 2010).

Material and Methods

Antibodies and reagents

The following antibodies were commercially obtained and used as stated:

Anoctamin 8 (WB 1:500, #HPA049206, Atlas Antibodies), ARHGAP33 (Western-blotting (WB) 1:500, #HPA030117, Atlas Antibodies), beta-Actin (WB 1:2000, #A2228, Sigma-Aldrich), cathepsin D (EM 1:50, #219361, Calbiochem), CD63/Lamp3 (EM 1:20, #M1544, Sanquin), claudin 3 (IF 1:200, #SAB4500435, Sigma-Aldrich), DNP (EM 1:6-1:30, #71-3500, Invitrogen), DPP4 (IF/FACS 1:100, #HBB3/775/42, DSHB; EM 1:10, #AF1180, R&D Systems), E-Cadherin (IF 1:200, EM 1:30, #610181, BD Bioscences), GALNT2 (WB 1:1000, #AF7507, Novus Biologicals), Lamp1 (IF 1:200, EM 1:10, #1D4B, DSHB), MTMR2 (WB 1:500, #sc-365184, Santa Cruz Biotechnology), PIP5K1C (WB 1:1000, #3296S, Cell Signaling Technology), syntaxin3 (IF 1:100, EM 1:10, #133750, Abcam), TM9SF4 (WB 1:1000, #sc-374473, Santa Cruz Biotechnology), TMEM110 (WB 1:1000, #NBP1-69238, Novus Biologicals), ZO-1 (EM 1:50, #61-7300 Zymed);

Secondary horse-radish peroxidase-coupled (HRP) goat anti–mouse and goat anti-rabbit (1:5000, Sigma-Aldrich) were used for WB and secondary Alexa Fluor-conjugated (Alexa Fluor 488 and 568) goat anti-mouse (1:1000, Life Technologies), goat anti-rabbit (1:1000, Life Technologies) were used for IF labelling. For labelling of actin filaments, we used phalloidin–Alexa Fluor 568 (1:500, Life Technologies) and for nuclear staining we used Hoechst 3342 (1:10,000, Thermo Fisher Scientific). Secondary antibodies conjugated to 5, 6, 10 or 15nm colloidal gold particles diluted to 1:50-150 for EM were from British Biocell Intl. and Aurion.

Plasmids and lentivirus production

For CRISPR/Cas9-mediated depletion, guide RNA (gRNA) targeting sequences for ARHGAP33 (5′-TCCACCGGTGCATATTTGAC-3′), TM9SF4 (5′-GCCCAGCAAGATAACCTACA-3′), Pip5k1c (5’- GAAGTTGGGCCATCGAGGTG -3’), Mtmr2 (5’- AGTCGAGGTGAAAATTCTTA -3’), Tmem110 (5’-GAGCAAGGTCCGCTACCGGA-3’), ANO8 (5’-CCGATGACCACACGCTGCTA-3’) and Galnt2 (5′-ACTGCGAGTGTAATGAGCAC-3′) were selected from the Geckov2-CRISPR library, according to their targeting efficiency in the primary CRISPR-screen (CRISPR Design; Zhang lab, Massachusetts Institute of Technology; Hsu et al., 2013). gRNAs were cloned into a lentiCRISPRv2 vector via BsmBI restriction enzyme sites. lentiCRISPRv2 was a gift from F. Zhang (Massachusetts Institute of Technology, Cambridge, MA; Addgene plasmid 52961; Sanjana et al., 2014). For the generation of knock-down cell lines, lentiviral plasmids were cotransfected using Lipofectamine LTX (Invitrogen)-transfection reagent together with pVSV-G and psPAX2 in the Hek293LTV producer cell line. Virus containing supernatants were collected after 48 and 72 h after

transfection and directly used for CaCo2 cell infection. 6 days after infection, cells were selected with 10 µg/ml puromycin (Sigma-Aldrich) or 20 µg/ml blasticidin S (Invitrogen). Depletion efficiency was verified via WB.

Cell culture

Hek293LTV, CaCo2 WT, and KI cells were cultured in DMEM (Sigma-Aldrich) containing high glucose, sodium pyruvate, 100 U/ml penicillin (Sigma-Aldrich), 100 µg/ml streptomycin (Sigma-Aldrich), 5% nonessential amino acids (Gibco), and 10% FBS (Gibco) in a humidified atmosphere with 5% CO2 at 37°C. For experiments requiring fully polarized growth conditions, CaCo2 cells were seeded on 24-mm or 75-mm filters (Costar Transwell; pore size of 0.4 µm; Corning) and cultured for 14–28 d. For 3D cyst assays, CaCo2 cells were cultivated and processed as described previously (Vogel et al., 2015b; Jaffe et al., 2008). For this purpose, 1-2x10^4/mL single cells were embedded in Matrigel (BD Biosiences, #356231) per well of an 8x chamber slide (Lab-Tek®-chamber slide, Sig ma) and grown for 7 days (Román-Fernández et al., 2018). Three biological and three technical replicates were performed.

TEER measurements

Transepithelial electric resistance (TEER) measurements were performed in CaCo2 wildtype and the generated KD-cell lines. TEER was measured using an STX2 electrode together with the EVOM epithelial volt-ohmmeter from World precision instruments. TEER measurements were performed on days 0, 4,7, 11, 14, and 19 after cells were seeded on transwell filters at confluence for polarization. The measurements were performed at three different areas on the filter inserts and calculated as described previously (Klee et al., 2020). Two biological and one technical replicate were performed.

Genome-wide CRISPR- screen

For the CRISPR-screen in polarized CaCo2 cells, we used the 2-vector system (lenti-guide Puro; Addgene #1000000049; Feng Zhang Lab, (Sanjana et al., 2014)). For the generation of the target CaCo2 cell line, we introduced the vector encoding Cas9 (lentiCas9-Blast) for stable expression with a lentivirus to CaCo2 cells.

For virus production containing the sgRNA library, HEK293T cells seeded to 150mm dishes were transfected with 21 µg of the human gRNA pooled library in lentiGuide-Puro (Addgene #1000000049), 15.75 µg of pSPAX2 and 5.25 µg of pVSV-G plasmids. Viral supernatants were collected after 36 h and 50 h and concentrated with Amicon ultra-15 centrifugation tubes (Merck). For storage and further usage samples were snap frozen in liquid nitrogen.

The CRISPR/Cas9 screen was performed as described in previous studies by (Hutter et al., 2020; Shalem et al., 2014). One biological and two technical replicates were performed. For

each replicate 2 x 10^8 CaCo2-Cas9 screen cells were transduced with a virus preparation containing 16 µg/mL polybrene at an MOI of 0.2 and seeded at a low density (10^7 cells/150 mm plate) to 20 150mm culture dishes. 72 hours after infection, selection with 10 µg Puromycin was started and cells were selected for 7 days. After 7 days of selection, surviving screen cells were pooled and evenly distributed to 100 mm culture dishes, to obtain confluent monolayers. The cells were then cultivated for polarization as confluent monolayers for 18 days. After 18 days, cells were detached with StemPro™ Accutase™ Cell Dissociation Reagent (Thermo Fisher Scientific, #A1110501) and stained for FACS. Thereby cell suspensions were washed after detachment 2x with ice cold PBS and subsequently incubated in PBS containing 1% FBS and anti-DPP4 antibody (1:100) on ice for 20 minutes. After incubation cells were washed 2x in ice cold PBS and then incubated with PBS containing 1% FBS and a secondary anti-mouse AlexaFluor-488 antibody (1:1000) on ice for 20 minutes. After the incubation, cells were washed 2x in ice cold PBS, resuspended in PBS containing 2% FBS and subjected to FACS sorting using an ARIA III (Becton Dickinson). For each replicate, approx. 1.5 Mio cells corresponding to the lowest 10% Alexa-488 (A-488-negative) of the total cell population was sorted. Unsorted cells were saved and used as control. Genomic DNA (gDNA) was isolated from sorted and unsorted cells using the Nucleospin Tissue Mini Kit (Macherey-Nagel) and sgRNA sequences were retrieved by a nested PCR approach that pre-amplified sgRNAs in a first round with primers specific to the lentiGuide-Puro construct (5'-AGAGGGCCTATTTCCCATGA-3') and added stagger bases, specific barcodes and the Illumina adapters in the second round. The PCR products were separated on a 1% agarose gel, purified by gel extraction, quantified and then pooled before sequencing on a Hiseq4000 (Illumina) in collaboration with the Biomedical Sequencing Facility (BSF, Vienna, Austria). Sequencing data were analyzed with the publically available online tools GenePattern (Chapman et al., 2006) and Galaxy (Afgan et al., 2018). Reads were first demultiplexed and trimmed followed by alignment of the sgRNA sequences to a reference using Bowtie2 (Langmead and Salzberg, 2012). SgRNAs enriched in the sorted A-488-negative populations were identified using the edgeR shRNaseq tool (Table CRISPR screen Analysis for Enriched sgRNAs in the A-488-negative; (Ritchie et al., 2014)).

Flow cytometry

To measure DPP4 levels at the surface of WT and respective KD cell lines, cells were seeded as confluent monolayers and polarized for 18 days on 6 well cell culture dishes. Subsequently, cells were detached and stained as mentioned above (*Genome-wide CRISPR-Screen*). After staining, cells were subjected to measurements at an Attune NxT Flow Cytometer (Invitrogen) and Data was analyzed with FloJo software (Becton Dickinson). Two biological and one technical replicate were performed.

Immunoblots

Total cell lysates were prepared and westernblot analysis was performed as described previously (Cattelani et al., 2021). Cells were washed in 1x cold PBS, scraped from respective culture-plates and pelleted with 1500xg for 5 min at 4°C. Cell pellets were resuspended in Lysis buffer (50 mM HEPES pH 8.0, 150 mM NaCl, 5 mM EDTA pH 8.0, 0.5 % NP-40, 50 mM NaF, 10 µg/mL Leupeptin, 0.4 mM Pefablock, 1 µ/mL Pepstatin, 10 µg/mL Aprotinin, 0.5 mM PMSF, 1 mM N3VO4) and lysed for 60 minutes on ice. Followingly, lysates were centrifuged at 13.000xg for 15 minutes and cleared lysate was obtained. Lysates were separated by SDS-Polyacrylamide Gel Electrophoresis (PAGE). Polyacrylamide gels were prepared consisting of stacking (125 mM Tris pH 6.8, 4% Acrylamide/Bis solution (37:5:1), 6% glycerol, 0.1% SDS, 0.075% APS, and 0.1% TEMED) and resolving gels (0.375 mM Tris pH 8.8, 7–15% Acrylamide/Bis solution (37:5:1), 0.1% SDS, 0.05% APS, and 0.05% TEMED). All SDS PAGE gels were run in 192 mM glycine, 25 mM Trisma Base, 0.1% SDS. After separation, the proteins were wet transferred onto 'Amersham™ Protran™0.2 µm NC' nitrocellulose membranes (GE10600002 Sigma-Aldrich Handels Gmbh, Vienna, Austria) at constant 80 V for 1,5 h. The wet transfer buffer contained 25 mM Tris, 192 mM glycine, 0.1% SDS, and 20% methanol (vol/vol), adjusted to pH 8.3. Membranes were subsequently blocked in 3% BSA (fraction V), 1 mM EDTA, 0.05% Tween20, and 0.02% NaN3, and probed with the respective antibodies.

Immunofluorescence microscopy

Immunofluorescence stainings on cells grown and polarized on glass-coverslips or of 3D cyst cultures were performed as described previously (Vogel et al., 2017b, 2015b). Briefly, for stainings of polarized 2D monolayers, cells grown on glass coverslips were fixed with 4%formaldehyde (made from paraformaldehyde) at room temperature for 3 hours or 100% methanol at -20°C for 5 minutes, respectively. Cells stained with anti-DPP4, anti-stx3, anti- HA and phalloidin, were fixed with formaldehyde, while for stainings with anti-ZO-1, anti-ECadherin, anti-clau3, anti-NaK-ATPase and anti-Moesin, cells were fixed with methanol. CaCo2 cysts were prepared for IF microscopy as described previously (Jaffe et al., 2008). Confocal stacks from monolayers/cysts mounted in Mowiol were taken on confocal fluorescence microscopes (SP5 and SP8; Leica) using a glycerol 63 x lense with a numerical aperture of 1.3 (Leica) on a Leica SP5 microscope and a glycerol 93 x lense with a numerical aperture of 1.3 on the Leica SP8 microscope, at room temperature. As recording softwares LASAF 2.7.3. (Leica) and LAS X (Leica) were used. All images were deconvolved using Huygens Professional Devonvolution and Analysis Software (Scientific Volume Imaging) and exported using Imaris 3D rendering (Bitplane) and finally adjusted for brightness and contrast using Fiji-ImageJ software.

Electron microscopy

Transmission EM for morphology of filter-grown, polarized monolayers included rapid cryo-immobilization through means of high-pressure freezing, followed by freeze-substitution and epoxy resin embedding as described previously (Vogel et al., 2015b; Ruemmele et al., 2010). Immunogold EM was described previously; in brief, polarized monolayers grown for 14 days in petri dishes were fixed with 4% formaldehyde or 4% formaldehyde plus 0.1% glutaraldehyde and processed for Tokuyasu-ultracryotomy (Vogel et al., 2017a; Tokuyasu, 1973). Optionally, cells were subjected to serum-stravation overnight, followed by incubation for 2 hours with DAMP ((Orci et al., 1986); 3-(2,4-Dinitroanilino)-3'amino-N-methylpropyl-amine, #D1552 from Molecular Probes; 30µM/l dissolved in serum-free medium) prior to aldehyde fixation. Analysis of thin sections was performed with a Philips CM120 (now ThermoFisher Scientific), equipped with a MORADA digital camera and iTEM-software (EMSIS, Münster Germany). Image contrast, brightness, greyscale and sharpness were adjusted with Photoshop CS6 (Adobe, San José, CA, USA). Two biological and three technical replicates were performed.

Scanning EM of filter-grown polarized monolayers was performed with a DSM 982 Gemini (ZEISS, Oberkochen, Germany) as described previously (Ruemmele et al., 2010); briefly, sample processing included chemical fixation, dehydration, critical point drying and sputter coating. Two biological and three technical replicates were performed.

GO-term analysis

For manual GO-term analysis, each of the 89 significantly enriched genes from out CRISPR-screen were subjected to a manual GO-term search using https://www.uniprot.org/ and https://www.ebi.ac.uk/QuickGO/annotations. For each gene, 3 GO-terms were listed, prioritizing most common GO-terms suggested by the QuickGO-Database and GO-terms indicating a relation to the secretory pathway, for each of the three categories, biological process (BP), molecular function (MF), cellular compartment (CC). According to commonalities in the individuals sets of GO-terms, genes were then grouped and graphically visualized using Affinity Designer.

Statistics and Software

The software used, if not already specified, were Affinity Designer (Version 1.9.3), Fiji/ImageJ (Version 2.1.0/1.53c), GraphPad Prism 9 (Version 9.1.0), Serial Cloner (Version 2.6); For the analysis and visualization of FACS-Data we used Flowjo (Becton Dickinson). Dot box plot graphs were generated and the unpaired Mann–Whitney U test was calculated using R (R Core Team (2021). R: A language and environment for statistical Computing. R Foundation for Statistical Computing, Vienna, Austria. URL https://www.R-project.org) and ggplot2 package.

Data availability

Next generation sequencing data was made available at https://doi.org/10.5061/dryad.m0cfxpp62.

Acknowledgements

We want to thank the Biomedical sequencing facility (BSF) at the Research Center for Molecular Medicine (CeMM) of the Austrian Academy of Science (ÖAW) in Vienna for their next-generation-sequencing (NGS) services, especially Jan Laine and Michael Schuster.

We thank Karin Gutleben, Barbara Witting and Angelika Flörl (Institute of Histology and Embryology, Medical University of Innsbruck), and Caroline Krebiehl (Institute of Cell Biology, Medical University of Innsbruck) for technical assistance.

We further thank the Austrian Academy of Science (ÖAW) for grating the DOC-Scholarship to Katharina MC Klee and thereby supporting this work. This research was funded in part by the Austrian Science Fund (FWF) [P35805] and the Jubiläumsfonds der Österreichischen Nationalbank (grant No. 18019). For the purpose of Open Access, the author has applied a CC BY public copyright licence to any Auhtor Accepted Manuscript (AAM) version arising from this submission.

The authors declare no competing financial interest.

Author contributions: Conceptualization, Katharina MC Klee, Georg F Vogel, Michael W Hess, Lukas A Huber; Methodology and Investigation, Katharina MC Klee, Michael W Hess, Kristian Pfaller, Michael Lohmüller, Biomedical sequencing facility (BMSF) Vienna; Formal Analysis, Writing- original Draft, Katharina MC Klee, Michael W Hess; Writing-Review and Editing, Michael W Hess, Georg F Vogel, Lukas A Huber; Supervision, Georg F Vogel, Lukas A Huber; Funding Acquisition, Georg F Vogel, Lukas A Huber, Katharina MC Klee;

References

Afgan, E., D. Baker, B. Batut, M. van den Beek, D. Bouvier, M. Ech, J. Chilton, D. Clements, N. Coraor, B.A. Grüning, A. Guerler, J. Hillman-Jackson, S. Hiltemann, V. Jalili, H. Rasche, N. Soranzo, J. Goecks, J. Taylor, A. Nekrutenko, and D. Blankenberg. 2018. The Galaxy platform for accessible, reproducible and collaborative biomedical analyses. *Nuc. Acids Res*. 46:W537–W544. doi:10.1093/NAR/GKY379.

Apodaca, G., L.I. Gallo, and D.M. Bryant. 2012. Role of membrane traffic in the generation of epithelial cell asymmetry. *Nat. Cell Biol.* 14:1235–1243. doi:10.1038/ncb2635.

De Araujo, M.E.G., A. Naschberger, B.G. Fürnrohr, T. Stasyk, T. Dunzendorfer-Matt, S. Lechner, S. Welti, L. Kremser, G. Shivalingaiah, M. Offterdinger, H.H. Lindner, L.A. Huber, and K. Scheffzek. 2017. Crystal structure of the human lysosomal mTORC1 scaffold complex and its impact on signaling. *Science (1979)*. 358:377–381. doi:10.1126/science.aao1583.

Bassaganyas, L., S.J. Popa, M. Horlbeck, C. Puri, S.E. Stewart, F. Campelo, A. Ashok, C.M. Butnaru, N. Brouwers, K. Heydari, J. Ripoche, J. Weissman, D.C. Rubinsztein, R. Schekman, V. Malhotra, K. Moreau, and J. Villeneuve. 2019. New factors for protein transport identified by a genome-wide CRISPRi screen in mammalian cells. *J. Cell Biol*. 218:3861–3879. doi:10.1083/jcb.201902028.

Bright, N.A., L.J. Davis, and J.P. Luzio. 2016. Endolysosomes Are the Principal Intracellular Sites of Acid Hydrolase Activity. *Curr. Biol*. 26:2233–2245. doi:10.1016/j.cub.2016.06.046.

Bryant, D.M., A. Datta, A.E. Rodríguez-Fraticelli, J. Peränen, F. Martín-Belmonte, and K.E. Mostov. 2010. A molecular network for de novo generation of the apical surface and lumen. *Nat. Cell Biol*. 12:1035–1045. doi:10.1038/ncb2106.

Canani, R.B., G. Terrin, G. Cardillo, R. Tomaiuolo, and G. Castaldo. 2010. Congenital diarrheal disorders: improved understanding of gene defects is leading to advances in intestinal physiology and clinical management. *J. Pediatr. Gastroenterol. Nutr*. 50:360–366. doi:10.1097/MPG.0B013E3181D135EF.

Cattelani, C., D. Lesiak, G. Liebscher, I.I. Singer, T. Stasyk, M.H. Wallnöfer, A.M. Heberle, C. Corti, M.W. Hess, K. Pfaller, M. Kwiatkowski, P.P. Pramstaller, A.A. Hicks, K. Thedieck, T. Müller, L.A. Huber, and M.E.G. de Araujo. 2021. The szt2 interactome unravels new functions of the kicstor complex. *Cells*. 10:1–30. doi:10.3390/cells10102711.

Chapman, S.J., C.C. Khor, F.O. Vannberg, N.A. Maskell, C.W. Davies, E.L. Hedley, S. Segal, C.E. Moore, K. Knox, N.P. Day, S.H. Gillespie, D.W. Crook, R.J. Davies, and A.V. Hill. 2006. GenePattern 2.0. *Nat. Genetics*. 38:500–501. doi:10.1038/ng0506-500.

Chung, G.H.C., J.J. Burden, M. Lorvellec, P. Gissen, and C.J. Stefan. 2020. ER-PM contacts regulate apical domain formation in hepatocytes. *bioRxiv*. doi:10.1101/2020.04.23.057521.

Cutz, E., J.M. Rhoads, B. Drumm, P.M. Shermann, P.R. Durie, and G.G. Forstner. 1989. Microvillus inclusion disease: an inherited defect of brush-border assembly and differentiation. *N. Engl. J. Med*. 320:646–651. doi:10.1056/NEJM198903093201006.

Denais, C., C.L. Dent, L. Southgate, J. Hoyle, D. Dafou, R.C. Trembath, and R.D. Machado. 2011. Dymeclin, the gene underlying Dyggve-Melchior-Clausen syndrome, encodes a protein integral to extracellular matrix and golgi organization and is associated with protein secretion pathways critical in bone development. *Hum. Mutat*. 32:231–239. doi:10.1002/HUMU.21413.

Dulcaux-Loras, R., C. Lebreton, J. Berthelet, F. Charbit-Henrion, O. Nicolle, C. Revenu, S. Waich, T. Valovka, A. Khiat, M. Rabant, C. Racine, C. Guerrera, J. Baptista, M. Mahe, M.W. Hess, B. Durel, N.

Lefort, C. Banal, M. Parisot, C. Talbotec, F. Lacaille, E. Ecochard-Dugelay, A.M. Demir, G.F. Vogel, L. Faivre, A. Rodrigues, D. Fowler, A.R. Janecke, T. Müller, L.A. Huber, F. Rodrigues-Lima, F. Ruemmele, H.H. Uhlig, F. del Bene, G. Michaux, N. Cerf-Bensussan, and M. Parlato. 2022. UNC45A deficiency causes microvillus inclusion disease-like phenotype by impairing myosin VB–dependent apical trafficking. *J. Clin. Inv*. *in press.*

Esteve, C., L. Francescatto, P.L. Tan, A. Bourchany, C. De Leusse, E. Marinier, A. Blanchard, P. Bourgeois, C. Brochier-Armanet, A.L. Bruel, A. Delarue, Y. Duffourd, E. Ecochard-Dugelay, G. Hery, F. Huet, P. Gauchez, E. Gonzales, C. Guettier-Bouttier, M. Komuta, C. Lacoste, R. Maudinas, K. Mazodier, Y. Rimet, J.B. Rivière, B. Roquelaure, S. Sigaudy, X. Stephenne, C. Thauvin-Robinet, J. Thevenon, J. Sarles, N. Levy, C. Badens, O. Goulet, J.P. Hugot, N. Katsanis, L. Faivre, and A. Fabre. 2018. Loss-of-Function Mutations in UNC45A Cause a Syndrome Associating Cholestasis, Diarrhea, Impaired Hearing, and Bone Fragility. *Am. J. Hum. Genet*. 102:364–374. doi:10.1016/J.AJHG.2018.01.009.

Fujita, M., F. Reinhart, and M. Neutra. 1990. Convergence of apical and basolateral endocytic pathways at apical late endosomes in absorptive cells of suckling rat ileum in vivo. *J. Cell Sci*. 97:385–394. doi:10.1242/jcs.97.2.385.

Gaisano, H.Y., M. Ghai, P.N. Malkus, L. Sheu, A. Bouquillon, M.K. Bennett, and W.S. Trimble. 1996. Distinct cellular locations of the syntaxin family of proteins in rat pancreatic acinar cells. *Mol. Biol. Cell*. 7:2019–2027. doi:10.1091/mbc.7.12.2019.

Hallermann, S. 2014. Calcium channels for endocytosis. *J. Physiol*. 592:3343. doi:10.1113/JPHYSIOL.2014.278838.

He, C., S. Han, Y. Chang, M. Wu, Y. Zhao, C. Chen, and X. Chu. 2021. CRISPR screen in cancer: status quo and future perspectives. *Am. J. Can. Res*. 11:1031–1050.

Hess, M.W., and L.A. Huber. 2021. Measuring lysosomal size and frequency by electron microscopy. *Meth. Cell Biol*. 164:47–61. doi:10.1016/BS.MCB.2020.10.019.

Homma, Y., R. Kinoshita, Y. Kuchitsu, P.S. Wawro, S. Marubashi, M.E. Oguchi, M. Ishida, N. Fujita, and M. Fukuda. 2019. Comprehensive knockout analysis of the Rab family GTPases in epithelial cells. *J. Cell Biol*. 218:2035–2050. doi:10.1083/JCB.201810134.

Hutter, K., M. Lohmüller, A. Jukic, F. Eichin, S. Avci, V. Labi, T.G. Szabo, S.M. Hoser, A. Hüttenhofer, A. Villunger, and S. Herzog. 2020. SAFB2 Enables the Processing of Suboptimal Stem-Loop Structures in Clustered Primary miRNA Transcripts. *Mol. Cell*. 78:876-889.e6. doi:10.1016/j.molcel.2020.05.011.

Jaffe, A.B., N. Kaji, J. Durgan, and A. Hall. 2008. Cdc42 controls spindle orientation to position the apical surface during epithelial morphogenesis. *J. Cell Biol*. 183:625–633. doi:10.1083/jcb.200807121.

Jha, A., W.Y. Chung, L. Vachel, J. Maleth, S. Lake, G. Zhang, M. Ahuja, and S. Muallem. 2019. Anoctamin 8 tethers endoplasmic reticulum and plasma membrane for assembly of Ca 2+ signaling complexes at the ER/PM compartment. *EMBO J*. 38:e101452. doi:10.15252/embj.2018101452.

Kampmann, M. 2018. CRISPRi and CRISPRa Screens in Mammalian Cells for Precision Biology and Medicine. *ACS Chemi. Biol*. 13:406–416. doi:10.1021/acschembio.7b00657.

Kim, Y., C.M. Ha, and S. Chang. 2013. SNX26, a GTPase-activating protein for Cdc42, interacts with PSD-95 protein and is involved in activity-dependent dendritic spine formation in mature neurons. *J. Biol. Chem*. 288:29453–29466. doi:10.1074/jbc.M113.468801.

Klee, K.M.C., A.R. Janecke, H.A. Civan, Š. Rosipal, P. Heinz-Erian, L.A. Huber, T. Müller, and G.F. Vogel. 2020. AP1S1 missense mutations cause a congenital enteropathy via an epithelial barrier defect. *Hum. Gen*. 139:1247–1259. doi:10.1007/S00439-020-02168-W/FIGURES/5.

Langmead, B., and S.L. Salzberg. 2012. Fast gapped-read alignment with Bowtie 2. *Nat. Methods*. 9:357–359. doi:10.1038/nmeth.1923.

Lebreton, S., S. Paladino, D. Liu, M. Nitti, J. von Blume, P. Pinton, and C. Zurzolo. 2021. Calcium levels in the Golgi complex regulate clustering and apical sorting of GPI-APs in polarized epithelial cells. *Proc. Natl. Acad. Sci. U S A*. 118: e2014709118. doi:10.1073/PNAS.2014709118/SUPPL_FILE/PNAS.2014709118.SAPP.PDF.

Levic, D.S., and M. Bagnat. 2021. Self-organization of apical membrane protein sorting in epithelial cells. *FEBS J*. doi:10.1111/FEBS.15882.

Levic, D.S., S. Ryan, L. Marjoram, J. Honeycutt, J. Bagwell, and M. Bagnat. 2020. Distinct roles for luminal acidification in apical protein sorting and trafficking in zebrafish. *J. Cell Biol*. 219:e201908225. doi:10.1083/JCB.201908225.

Li, Q., Z. Zhou, Y. Sun, C. Sun, K. Klappe, and S.C.D. van IJzendoorn. 2022. A functional relationship between UNC45A and MYO5B connects two rare diseases with shared enteropathy. *Cell. Mol. Gastroenterol. Hepatol*. S2352-345X(22)00071-6. doi:10.1016/J.JCMGH.2022.04.006.

Li, X., S.H. Low, M. Miura, and T. Weimbs. 2002. SNARE expression and localization in renal epithelial cells suggest mechanism for variability of trafficking phenotypes. *Am. J. Phys. - Renal Phys*. 283:F1111-1122. doi:10.1152/ajprenal.00185.2002.

Low, S.H., S.J. Chapin, T. Weimbs, L.G. Kömüves, M.K. Bennett, and K.E. Mostov. 1996. Differential localization of syntaxin isoforms in polarized Madin-Darby canine kidney cells. *Mol. Biol. Cell*. 7:2007–2018. doi:10.1091/mbc.7.12.2007.

Lozupone, F., M. Borghi, F. Marzoli, T. Azzarito, P. Matarrese, E. Iessi, G. Venturi, S. Meschini, A. Canitano, R. Bona, A. Cara, and S. Fais. 2015. TM9SF4 is a novel V-ATPase-interacting protein that modulates tumor pH alterations associated with drug resistance and invasiveness of colon cancer cells. *Oncogene.* 34:5163–5174. doi:10.1038/onc.2014.437.

Martin-Belmonte, F., A. Gassama, A. Datta, W. Yu, U. Rescher, V. Gerke, and K. Mostov. 2007. PTEN-Mediated Apical Segregation of Phosphoinositides Controls Epithelial Morphogenesis through Cdc42. *Cell*. 128:383–397. doi:10.1016/j.cell.2006.11.051.

Medina, D.L., S. Di Paola, I. Peluso, A. Armani, D. De Stefani, R. Venditti, S. Montefusco, A. Scotto-Rosato, C. Prezioso, A. Forrester, C. Settembre, W. Wang, Q. Gao, H. Xu, M. Sandri, R. Rizzuto, M.A. De Matteis, and A. Ballabio. 2015. Lysosomal calcium signaling regulates autophagy via calcineurin and TFEB. *Nat. Cell Biol*. 17:288. doi:10.1038/NCB3114.

Moremen, K.W., M. Tiemeyer, and A. v. Nairn. 2012. Vertebrate protein glycosylation: Diversity, synthesis and function. *Nat. Rev. Mol. Cell Biol*. 13:448–462. doi:10.1038/nrm3383.

Müller, T., M.W. Hess, N. Schiefermeier, K. Pfaller, H.L. Ebner, P. Heinz-Erian, H. Ponstingl, J. Partsch, B. Röllinghoff, H. Köhler, T. Berger, H. Lenhartz, B. Schlenck, R.J. Houwen, C.J. Taylor, H. Zoller, S. Lechner, O. Goulet, G. Utermann, F.M. Ruemmele, L.A. Huber, and A.R. Janecke. 2008. MYO5B mutations cause microvillus inclusion disease and disrupt epithelial cell polarity. *Nat Genet*. 40:1163–1165. doi:10.1038/ng.225.

Nakazawa, T., R. Hashimoto, K. Sakoori, Y. Sugaya, A. Tanimura, Y. Hashimotodani, K. Ohi, H. Yamamori, Y. Yasuda, S. Umeda-Yano, Y. Kiyama, K. Konno, T. Inoue, K. Yokoyama, T. Inoue, S. Numata, T. Ohnuma, N. Iwata, N. Ozaki, H. Hashimoto, M. Watanabe, T. Manabe, T. Yamamoto, M. Takeda, and M. Kano. 2016. Emerging roles of ARHGAP33 in intracellular trafficking of TrkB and pathophysiology of neuropsychiatric disorders. *Nat. Comm*. 7:10594. doi:10.1038/NCOMMS10594.

Orci, L., M. Ravazzola, M. Amherdt, O. Madsen, A. Perrelet, J.D. Vassalli, and R.G. Anderson. 1986. Conversion of proinsulin to insulin occurs coordinately with acidification of maturing secretory vesicles. *J. Cell Biol*. 103:2273–2281. doi:10.1083/jcb.103.6.2273.

Perrin, J., M. le Coadic, A. Vernay, M. Dias, N. Gopaldass, H. Ouertatani-Sakouhi, and P. Cosson. 2015. TM9 family proteins control surface targeting of glycine-rich transmembrane domains. *J. Cell Sci*. 128:2269–2277. doi:10.1242/jcs.164848.

Phillips, A.D., M. Szafranski, L.Y. Man, and W.J. Wall. 2000. Periodic acid-Schiff staining abnormality in microvillous atrophy: Photometric and ultrastructural studies. *J. Ped. Gastroenterol. Nutr*. 30:34–42. doi:10.1097/00005176-200001000-00015.

Popa, S., J. Villeneuve, S. Stewart, E.P. Garcia, A.P. Harrison, and K. Moreau. 2020. Genome-wide CRISPR screening identifies new regulators of glycoprotein secretion. *Well. Open Res*. 4:119. doi:10.12688/wellcomeopenres.15232.1.

Quintana, A., V. Rajanikanth, S. Farber-Katz, A. Gudlur, C. Zhang, J. Jing, Y. Zhou, A. Rao, and P.G. Hogan. 2015. TMEM110 regulates the maintenance and remodeling of mammalian ER-plasma membrane junctions competent for STIM-Orai signaling. *Proc. Natl. Acad. Sci. U S A*. 112:E7083–E7092. doi:10.1073/pnas.1521924112.

Remis, N.N., T. Wiwatpanit, A.J. Castiglioni, E.N. Flores, J.A. Cantú, and J. García-Añoveros. 2014. Mucolipin Co-deficiency Causes Accelerated Endolysosomal Vacuolation of Enterocytes and Failure-to-Thrive from Birth to Weaning. *PLoS Genetics*. 10:e1004833 doi:10.1371/journal.pgen.1004833.

Ritchie, M.E., Z. Dai, J.M. Sheridan, L.J. Gearing, D.L. Moore, S. Su, R.A. Dickins, and M.E. Blewitt. 2014. ShRNA-seq data analysis with edgeR. *F1000Res*. 3:1–8. doi:10.12688/f1000research.3928.1.

Rodriguez-Boulan, E., G. Kreitzer, and A. Müsch. 2005. Organization of vesicular trafficking in epithelia. *Nat. Rev. Mol. Cell Biol*. 6:233–247. doi:10.1038/nrm1593.

Rodriguez-Boulan, E., and I.G. Macara. 2014. Organization and execution of the epithelial polarity programme. *Nat. Rev. Mol. Cell Biol*. 15:225–242. doi:10.1038/nrm3775.

Román-Fernández, A., and D.M. Bryant. 2016. Complex Polarity: Building Multicellular Tissues Through Apical Membrane Traffic. *Traffic*. 17:1244–1261. doi:10.1111/TRA.12417.

Román-Fernández, Á., J. Roignot, E. Sandilands, M. Nacke, M.A. Mansour, L. McGarry, E. Shanks, K.E. Mostov, and D.M. Bryant. 2018. The phospholipid PI(3,4)P2 is an apical identity determinant. *Nat. Comm*. 9:5041. doi:10.1038/S41467-018-07464-8.

Ruemmele, F.M., T. Müller, N. Schiefermeier, H.L. Ebner, S. Lechner, K. Pfaller, C.E. Thöni, O. Goulet, F. Lacaille, J. Schmitz, V. Colomb, F. Sauvat, Y. Revillon, D. Canioni, N. Brousse, G. de Saint-Basile, J. Lefebvre, P. Heinz-Erian, A. Enninger, G. Utermann, M.W. Hess, A.R. Janecke, and L.A. Huber. 2010. Loss-of-function of MYO5B is the main cause of microvillus inclusion disease: 15 Novel mutations and a CaCo-2 RNAi cell model. *Hum. Mut*. 31:544–551. doi:10.1002/humu.21224.

Ruemmele, F.M., J. Schmitz, and O. Goulet. 2006. Microvillous inclusion disease (microvillous atrophy). *Orphanet J. Rare Dis*. 1:22. doi:10.1186/1750-1172-1-22.

Sanjana, N.E., O. Shalem, and F. Zhang. 2014. Improved vectors and genome-wide libraries for CRISPR screening. *Nat. Methods*. 11:783–784. doi:10.1038/nmeth.3047.

Sbano, L., M. Bonora, S. Marchi, F. Baldassari, D.L. Medina, A. Ballabio, C. Giorgi, and P. Pinton. 2017. TFEB-mediated increase in peripheral lysosomes regulates store-operated calcium entry. *Sci. Rep.* 7:1–13. doi:10.1038/srep40797.

Schuck, S., and K. Simons. 2004. Polarized sorting in epithelial cells: raft clustering and the biogenesis of the apical membrane. *J Cell Sci*. 117:5955–5964. doi:10.1242/JCS.01596.

Schuster, S., M. Rivalan, U. Strauss, L. Stoenica, T. Trimbuch, N. Rademacher, S. Parthasarathy, D. Lajkó, C. Rosenmund, S.A. Shoichet, Y. Winter, V. Tarabykin, and M. Rosário. 2015. NOMA-GAP/ARHGAP33 regulates synapse development and autistic-like behavior in the mouse. *Mol. Psych.* 20:1120–1131. doi:10.1038/mp.2015.42.

Shalem, O., N.E. Sanjana, E. Hartenian, X. Shi, D.A. Scott, T.S. Mikkelsen, D. Heckl, B.L. Ebert, D.E. Root, J.G. Doench, and F. Zhang. 2014. Genome-scale CRISPR-Cas9 knockout screening in human cells. *Science (1979)*. 343:84–87. doi:10.1126/science.1247005.

Shalem, O., N.E. Sanjana, and F. Zhang. 2015. High-throughput functional genomics using CRISPR-Cas9. *Nat. Rev. Genetics*. 16:299–311. doi:10.1038/nrg3899.

Stewart, S.E., S.A. Menzies, S.J. Popa, N. Savinykh, A.P. Harrison, P.J. Lehner, and K. Moreau. 2017. A genome-wide CRISPR screen reconciles the role of N-linked glycosylation in galectin-3 transport to the cell surface. *J. of Cell Sci*. 130:3234–3247. doi:10.1242/jcs.206425.

Thiagarajah, J.R., D.S. Kamin, S. Acra, J.D. Goldsmith, J.T. Roland, W.I. Lencer, A.M. Muise, J.R. Goldenring, Y. Avitzur, and M.G. Martín. 2018. Advances in Evaluation of Chronic Diarrhea in Infants. *Gastroenterology*. 154:2045. doi:10.1053/J.GASTRO.2018.03.067.

Tokuyasu, K.T. 1973. A technique for ultracryotomy of cell suspensions and tissues. *J. Cell. Biol*. 57:551–565. doi:10.1083/JCB.57.2.551.

Vernay, A., O. Lamrabet, J. Perrin, and P. Cosson. 2018. TM9SF4 levels determine sorting of transmembrane domains in the early secretory pathway. *J. Cell Sci*. 131:jcs220830. doi:10.1242/jcs.220830.

Vogel, G.F., H.L. Ebner, M.E.G. de Araujo, T. Schmiedinger, O. Eiter, H. Pircher, K. Gutleben, B. Witting, D. Teis, L.A. Huber, and M.W. Hess. 2015a. Ultrastructural Morphometry Points to a New Role for LAMTOR2 in Regulating the Endo/Lysosomal System. *Traffic*. 16:617–634. doi:10.1111/TRA.12271.

Vogel, G.F., A.R. Janecke, I.M. Krainer, K. Gutleben, B. Witting, S.G. Mitton, S. Mansour, A. Ballauff, J.T. Roland, A.C. Engevik, E. Cutz, T. Müller, J.R. Goldenring, L.A. Huber, and M.W. Hess. 2017a. Abnormal Rab11-Rab8-vesicles cluster in enterocytes of patients with microvillus inclusion disease. *Traffic*. 18:453–464. doi:10.1111/tra.12486.

Vogel, G.F., K.M.C. Klee, A.R. Janecke, T. Müller, M.W. Hess, and L.A. Huber. 2015b. Cargo-selective apical exocytosis in epithelial cells is conducted by Myo5B, Slp4a, Vamp7, and Syntaxin 3. *J. Cell Biol*. 211:587–604. doi:10.1083/jcb.201506112.

Vogel, G.F., J.M. van Rijn, I.M. Krainer, A.R. Janecke, C. Posovszky, M. Cohen, C. Searle, P. Jantchou, J.C. Escher, N. Patey, E. Cutz, T. Müller, S. Middendorp, M.W. Hess, and L.A. Huber. 2017b. Disrupted apical exocytosis of cargo vesicles causes enteropathy in FHL5 patients with Munc18-2 mutations. *JCI Insight*. 2:e94564. doi:10.1172/jci.insight.94564.

Wandall, H.H., H. Hassan, E. Mirgorodskaya, A.K. Kristensen, P. Roepstorff, E.P. Bennett, P.A. Nielsen, M.A. Hollingsworth, J. Burchell, J. Taylor-Papadimitriou, and H. Clausen. 1997. Substrate specificities of three members of the human UDP-N-acetyl-α- D-galactosamine:polypeptide N-acetylgalactosaminyltransferase family, GalNAc- T1, -T2, and -T3. *J. Biol. Chem*. 272:23503–23514. doi:10.1074/jbc.272.38.23503.

Wang, H., A.K. Bayram, R. Sprute, O. Ozdemir, E. Cooper, M. Pergande, S. Efthymiou, I. Nedic, N. Mazaheri, K. Stumpfe, R.A. Malamiri, G. Shariati, J. Zeighami, N. Bayram, S.K. Naghibzadeh, M. Tajik, M. Yaşar, A.S. Güven, F. Bibi, T. Sultan, V. Salpietro, H. Houlden, H. Per, H. Galehdari, B. Shalbafan, Y. Jamshidi, and S. Cirak. 2019. Genotype-phenotype correlations in charcot-marie-tooth disease due to mtmr2 mutations and implications in membrane trafficking. *Front. Neurosc*. 13:974. doi:10.3389/FNINS.2019.00974/FULL.

Weimbs, T., S.H. Low, S.J. Chapin, and K.E. Mostov. 1997. Apical targeting in polarized epithelial cells: There's more afloat than rafts. *Trends Cell Biol*. 7:393–399. doi:10.1016/S0962-8924(97)01130-6.

Weisz, O.A., and E. Rodriguez-Boulan. 2009. Apical trafficking in epithelial cells: Signals, clusters and motors. *J. Cell Sci*. 122:4253–4266. doi:10.1242/jcs.032615.

Wiegerinck, C.L., A.R. Janecke, K. Schneeberger, G.F. Vogel, D.Y. Van Haaften-Visser, J.C. Escher, R. Adam, C.E. Thöni, K. Pfaller, A.J. Jordan, C.A. Weis, I.J. Nijman, G.R. Monroe, P.M. Van Hasselt, E. Cutz, J. Klumperman, H. Clevers, E.E.S. Nieuwenhuis, R.H.J. Houwen, G. Van Haaften, M.W. Hess, L.A. Huber, J.M. Stapelbroek, T. Müller, and S. Middendorp. 2014. Loss of syntaxin 3 causes variant microvillus inclusion disease. *Gastroenterology*. 147:65-68.e10. doi:10.1053/j.gastro.2014.04.002.

Wilson, J.M., J.A. Whitney, and M.R. Neutra. 1991. Biogenesis of the apical endosome-lysosome complex during differentiation of absorptive epithelial cells in rat ileum. *J. Cell Sci*. 100:133–143. doi:10.1242/JCS.100.1.133.

Xu, W., M. Jin, W. Huang, H. Wang, R. Hu, J. Li, and Y. Cao. 2019. Apical PtdIns(4,5)P2 is required for ciliogenesis and suppression of polycystic kidney disease. *FASEB J*. 33:2848–2857. doi:10.1096/fj.201800385RRR.

Yamaji, T., T. Sekizuka, Y. Tachida, C. Sakuma, K. Morimoto, M. Kuroda, and K. Hanada. 2019. A CRISPR Screen Identifies LAPTM4A and TM9SF Proteins as Glycolipid-Regulating Factors. *iScience*. 11:409–424. doi:10.1016/j.isci.2018.12.039.

Yamoto, M., M. Alganabi, S. Chusilp, D. Lee, Y. Yazaki, C. Lee, B. Li, and A. Pierro. 2020. Lysosomal overloading and necrotizing enterocolitis. *Ped. Surgery Int*. 36:1157–1165. doi:10.1007/S00383-020-04724-X/FIGURES/6.

Yordanov, T.E., V.E.B. Hipolito, G. Liebscher, G.F. Vogel, T. Stasyk, C. Herrmann, S. Geley, D. Teis, R.J. Botelho, M.W. Hess, and L.A. Huber. 2019. Biogenesis of lysosome-related organelles complex-1 (BORC) regulates late endosomal/lysosomal size through PIKfyve-dependent phosphatidylinositol-3,5-bisphosphate. *Traffic*. 20:674–696. doi:10.1111/tra.12679.

Zhu, Y., F. Feng, G. Hu, Y. Wang, Y. Yu, Y. Zhu, W. Xu, X. Cai, Z. Sun, W. Han, R. Ye, D. Qu, Q. Ding, X. Huang, H. Chen, W. Xu, Y. Xie, Q. Cai, Z. Yuan, and R. Zhang. 2021. A genome-wide CRISPR screen identifies host factors that regulate SARS-CoV-2 entry. *Nat. Comm*. 12:961. doi:10.1038/s41467-021-21213-4.

Zurzolo, C., and K. Simons. 2016. Glycosylphosphatidylinositol-anchored proteins: Membrane organization and transport. *Biochim. Biophys. Acta - Biomembranes*. 1858:632–639. doi:10.1016/j.bbamem.2015.12.018.

Abbreviations

CaCo2 caucasian colorectal adenocarcinoma 2

CODE congenital diarrhea and enteropathy

DAMP 3-(2,4-Dinitroanilino)-3'amino-N-methylpropyl-amine

DPP4 Dipeptidylpeptidase 4

GO gene ontology

KD knock-down

KEGG Kyoto Encyclopedia of Genes and Genomes

MDCK madine darby canine kidney

MVI microvillus inclusion

MVID microvillus inclusion disease

TEER transepithelial electric resistance

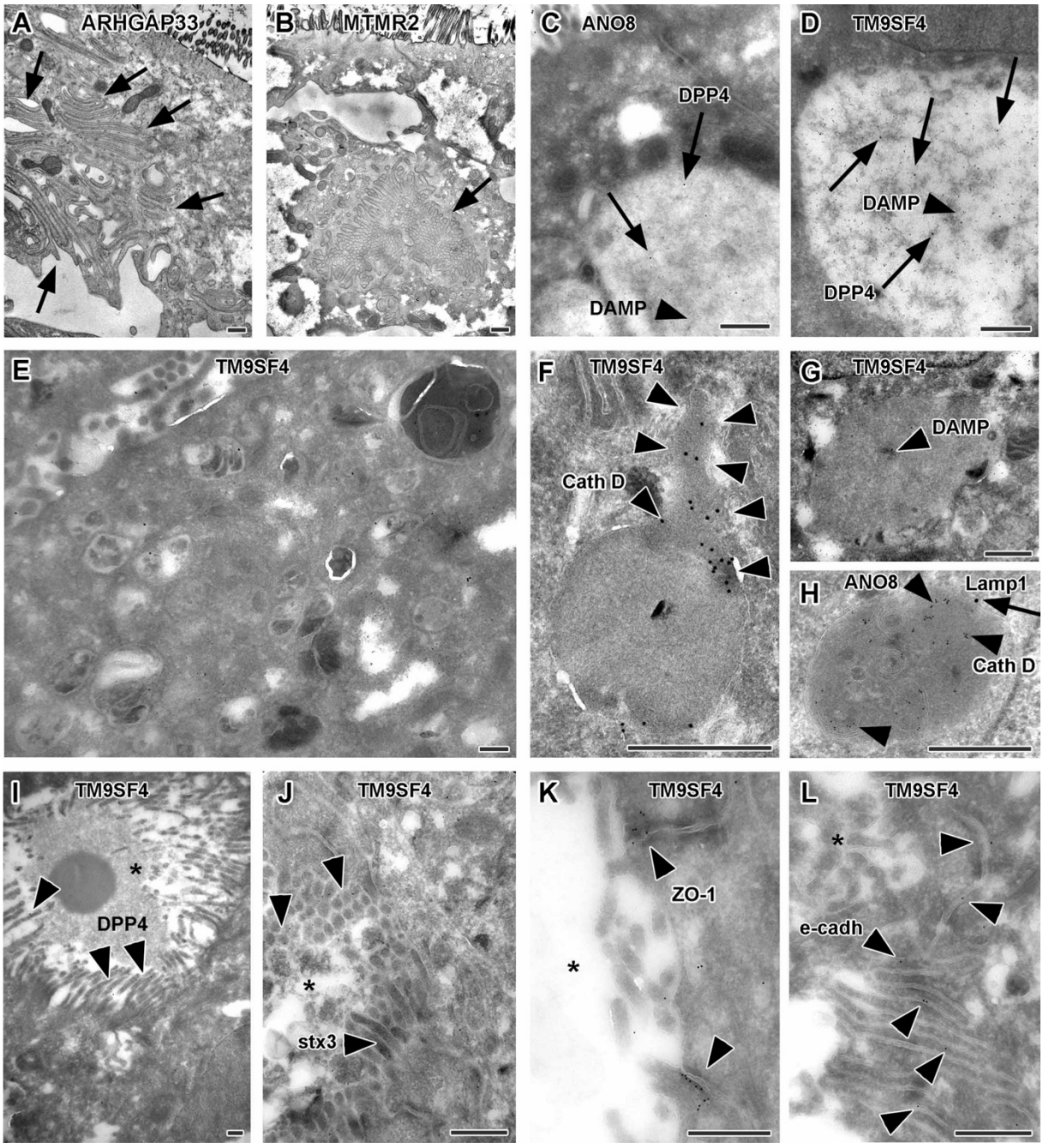

Figure S1. Complementary ultrastructure and immunoelectron microscopy on the phenotype of selected, polarized KD cells. Scale = 500 nm. A. Paracellular microvilli a/o numerous interdigitations in cryo-fixed ARHGAP33 KD cells. **B.** Intracellular microvillar cluster in cryo-fixed MTMR2 KD cell. **C.** Mislocalized DPP4 (arrows) in a huge, acidic (i.e., DAMP-positive: arrow head) compartment in ANO8 KD cell. **D.** Mislocalized DPP4 (arrows) in a huge DAMP-positive (arrow head) compartment in TM9SF4 KD cell. **E-H.** Normal late endosomal and lysosomal organelles as observed after serum starvation overnight. **E.** Overview on TM9SF4 KD cell. **F.** Reformed lysosome with cathepsin D immunogold label concentrated at its tubular part (outlined by arrow heads) in TM9SF4 KD cell. **G.** Weak DAMP-immunogold label (arrow head) within newly formed lysosome/protolysosome in TM9SF4 KD cell. **H.** Lamp1 (arrow) and cathepsin D (arrow heads) immunogold label in normal lysosome in ANO8 KD cell.

I. Ectopic DPP4 immunogold label (arrow heads) at basolateral, paracellular microvilli in TM9SF4 KD cell. **J.** Ectopic stx3 immunogold label (arrow heads) at basolateral, paracellular microvilli TM9SF4 KD cell. **K.** ZO1 immunogold label (arrow heads) at ectopic, basolateral tight junctions associated with paracellular microvillar spot (asterisk marks intercellular space) in TM9SF4 KD cell culture. **L.** E-cadherin immunogold label (arrow heads) at basolateral adherens junctions adjacent to a paracellular microvillar spot (asterisk marks intercellular space) in TM9SF4 KD cell culture.